

# ERA report series



## 21 CM-SAF Visiting Scientist Activity CM\_VS14\_01 Report: Characterisation of SSM/T-2 radiances using ERA-Interim and other reanalyses

---

Shinya Kobayashi<sup>1, 2</sup>, Paul Poli<sup>3</sup> and Viju John<sup>4, 5</sup>

<sup>1</sup> EUMETSAT CM-SAF Visiting Scientist

<sup>2</sup> Japan Meteorological Agency, Tokyo, Japan

<sup>3</sup> ECMWF Research Department

<sup>4</sup> Met Office, Exeter, UK

<sup>5</sup> EUMETSAT, Darmstadt, Germany

Series: ERA Report Series

A full list of ECMWF Publications can be found on our web site under:  
<http://www.ecmwf.int/en/research/publications>

© Copyright 2015

European Centre for Medium Range Weather Forecasts  
Shinfield Park, Reading, Berkshire RG2 9AX, England

Literary and scientific copyrights belong to ECMWF and are reserved in all countries. This publication is not to be reprinted or translated in whole or in part without the written permission of the Director. Appropriate non-commercial use will normally be granted under the condition that reference is made to ECMWF.

The information within this publication is given in good faith and considered to be true, but ECMWF accepts no liability for error, omission and for loss or damage arising from its use.

## Abstract

Satellite observations from microwave humidity sounders provide almost global and all-sky coverage except in thick cloud conditions. For climate applications, they have the potential to complement the coverage offered by existing tropospheric humidity datasets based on radiosonde observations (mainly over land) or satellite infrared observations (limited to cloud-free regions). Operational observations of microwave humidity sounders began in the early 1990s, with the Special Sensor Microwave Water Vapor Profiler (SSM/T-2). They have been continued since, with the Advanced Microwave Sounding Unit-B, the Microwave Humidity Sounder, and now the Advanced Technology Microwave Sounder. Among all of these, the SSM/T-2 data have been so far underused, both for numerical weather prediction and climate applications. As a consequence, expertise and accrued knowledge from use of these data is limited. In this study, SSM/T-2 radiances are characterised using the European Centre for Medium-Range Weather Forecasts (ECMWF) Interim Reanalysis (ERA-Interim), the ECMWF pilot reanalysis of the 20th-century assimilating surface observations only (ERA-20C) and the Japanese 55-year Reanalysis (JRA-55). The aims of the present study are to assess SSM/T-2 data quality, and potentially identify issues in the SSM/T-2 data that need to be solved before using it for climate monitoring and data assimilation.

First, the results obtained in the present study bring new light to the problem of the “unspecified” polarisation state of SSM/T-2. Comparing observations with simulations, we conclude that the antenna was oriented towards horizontal (not vertical) polarisation in the limit of nadir viewing. Second, the study reveals several issues that need to be taken into account when producing fundamental climate data records from the SSM/T-2 measurements, or assimilating them into future reanalyses. (1) Data from the Defence Meteorological Satellite Program (DMSP) 14 spacecraft suffer from large geolocation errors. (2) The measurements before 1994 contain unphysical values at quasi-periodic positions; the three outermost scans feature abnormally large departures; DMSP 15 data are unstable for all channels after November 2001 when the measurements of channel 4 degrade significantly. (3) There is a steady inter-satellite bias of 0.5 to 1 K between brightness temperatures from DMSP 12 and DMSP 14 in all channels. (4) An off-line cloud filtering method using tropospheric humidity channels is not as effective for cloud particles and rain drops in the lower troposphere as for ice clouds. Also, the results indicate that ERA-Interim matches SSM/T-2 183 GHz observations within 2–3 K of standard deviation.

Consequently, in order to use SSM/T-2 data most effectively for climate applications or for reanalysis, it is recommended to: (1) compute geolocation error corrections, (2) blacklist poor quality data, (3) apply inter-satellite recalibration, or, for reanalysis, an automated, e.g., variational, bias correction, and (4) improve cloud filtering methods, or, for reanalysis applications, consider an all-sky assimilation scheme that explicitly takes into account the scattering effect of hydrometeors in radiative transfer simulations.

This study also reports on a second set of computations, carried out after correcting some of the problems identified in the first computations. The fit between observed and simulated brightness temperatures is improved significantly as a result, with SSM/T-2 observations from the 150 GHz channels matching ERA-Interim computations within  $\pm 1$  K in the mean. This highlights the importance of accurate reference data and radiative transfer models for error characterisation, and the necessity of an iterative process in such calculations in order to enhance understanding of the error characteristics.

The SSM/T-2 observation data processed in this study, as well as corresponding radiative transfer simulations computed from reanalyses, are available from ECMWF Meteorological Archival and Retrieval System (MARS) for further research applications.

## 1 Introduction

Tropospheric water vapour plays an important role in regulating the energy balance of the surface and top of the atmosphere, provides a key feedback mechanism in the greenhouse effect, and is essential to the formation of clouds and precipitation (Hartmann *et al.*, 2013). It is crucial to have high quality tropospheric humidity Climate Data Records (CDRs) in order to understand the feedback mechanism and monitor its variability. Satellite observations from microwave humidity sounders provide almost global and all-sky coverage except in thick cloud conditions, and thereby have potential to complement the coverage limitations of existing tropospheric humidity datasets: radiosonde observations are mainly over land, and satellite infrared observations are limited to cloud-free regions (e.g. John *et al.*, 2011). Operational observations of microwave humidity sounders began with the Special Sensor Microwave Water Vapor Profiler (SSM/T-2) on the Defence Meteorological Satellite Program (DMSP) satellites in the early 1990's and continue with the Advanced Microwave Sounding Unit (AMSU)-B on the National Oceanic and Atmospheric Administration (NOAA) satellites (since 1998), the Microwave Humidity Sounder (MHS) on NOAA and Metop satellites (since 2005), and now the Advanced Technology Microwave Sounder (ATMS) on the Suomi National Polar-orbiting Partnership (NPP) satellite (since 2011). As a first step towards creating a high quality tropospheric humidity dataset from these measurements, the European Organisation for the Exploitation of Meteorological Satellites (EUMETSAT) Satellite Application Facility on Climate Monitoring (CM-SAF) has been working to produce fundamental climate data records (FCDRs), which consists of error characterised and bias adjusted radiances. Regarding SSM/T-2, this effort was also supported by a European Union Seventh Framework Programme (EU FP7), ERA-CLIM.

The AMSU-B, MHS, and ATMS data have been used by Numerical Weather Prediction (NWP) community and the error characteristics of these measurements are known to some extent. On the other hand, the SSM/T-2 data are underused both for NWP and for climate applications; consequently, expertise on these data is very limited. In order to quantitatively assess error characteristics of the SSM/T-2 data, high quality reference data are necessary for validation. However, such observations are rarely available, especially for the period before 1998 when the AMSU-B observations began. An alternative approach is to compare with equivalent brightness temperatures computed from a realistic NWP system. Several useful insights on characterisations of satellite microwave instruments have been obtained from differences between observations and estimates from NWP systems (e.g. Lu *et al.*, 2011; Lu and Bell, 2014) and reanalyses (e.g. Poli *et al.*, 2015).

In this report, we present results of characterisation of SSM/T-2 radiances using the European Centre for Medium-Range Weather Forecasts (ECMWF) Interim Reanalysis (ERA-Interim; Dee *et al.*, 2011), the ECMWF pilot reanalysis of the 20th-century assimilating surface observations only (ERA-20C; Poli *et al.*, 2013) and the Japanese 55-year Reanalysis (JRA-55; Kobayashi *et al.*, 2015). The SSM/T-2 dataset and reanalysis data are outlined in section 2. The radiative transfer calculations conducted in this study are presented in section 3. Section 4 reviews the error characteristics of SSM/T-2 measurements. Section 5 shows the results of a second series of computations, performed to apply lessons learnt and correct some of the problems identified in the first computations. Conclusions and recommendations are presented in section 6.

## 2 Data

### 2.1 SSM/T-2

The SSM/T-2 instrument is a five channel passive microwave sensor that operates in the 90-190 GHz frequency band (Galín *et al.*, 1993). It samples with 3 channels the emission in the 183.31 GHz water vapour rotational-transition band, allowing thus for atmospheric water vapor profile retrievals.

It is the first operational microwave humidity sounder, flown on 4 DMSP satellites (DMSP 11, 12, 14 and 15) to monitor this frequency. Emission at or near the other low-frequency water vapour rotational-transition band of 22.23 GHz, was sensed as early as 1972 by the Microwave Spectrometer (NEMS) on Nimbus-5, followed by the Scanning Microwave Spectrometer (SCAMS) on Nimbus-6, the Scanning Multichannel Microwave Radiometer (SMMR) on Nimbus-7 and Seasat, the Special Sensor Microwave/Imager (SSM/I) on several DMSP satellites after 1987, and several Microwave Radiometer (MWR) instruments employed in conjunction with sea-level altimeters (e.g., on European Remote Sensing Satellites (ERS)-1, and -2, Envisat, Jason-1, -2 and -3, but also Russian satellites of the Okean series). However, given radiometric capabilities, the 22 GHz line is not opaque enough to allow sub-sampling, and hence measurements at this frequency or nearby only allow retrieving total column water, and no vertical profile (Kakar, 1983).

The SSM/T-2 data considered in this study cover the period from 1992 to 2008. Therefore, tropospheric humidity datasets for over 20 years, continuing into the present, could be created in theory, by combining these data with similar measurements from AMSU-B, MHS, ATMS, the Special Sensor Microwave Imager/Sounder (SSMIS) and MTVZA-GY on NOAA, Metop, Suomi NPP and the future Joint Polar Satellite System (JPSS), DMSP, and Russian Meteor series. A first step in this direction is to assess the quality of the underlying radiance brightness temperatures, so as to possibly consider a Fundamental Climate Data Record (FCDR) of the 183.31 GHz band.

Prior to this study, the full set of Level 1 SSM/T-2 data were obtained originally from NOAA National Geophysical Data Center (NGDC; <http://www.ngdc.noaa.gov/eog/sensors/ssmt2.html>) and converted into the NetCDF format with some additional quality information (Chung and John, 2013). In the present study, we further convert the data into the ODB format and archive them into the ECMWF Meteorological Archive and Retrieval System (MARS) archive. A detailed list of parameters in SSM/T-2 ODB files and access instructions to those files are given in appendices A and B respectively.

Table 1 shows channel characteristics for SSM/T-2 and other instruments measuring passive radiation near the 183.31 GHz band of water vapour. Note that SSM/T-2 has larger fields of view (FOVs) than the others. Channels 1-3 of SSM/T-2 are the tropospheric humidity profiling channels; channels 4 and 5 are window channels and are used to filter rainy scenes (Ferraro *et al.*, 2000) which obfuscate retrieval of tropospheric humidity.

Table 1. Channel characteristics for SSM/T-2, AMSU-B, MHS, ATMS, SSMIS, and MTVZA.

Ch	Centre frequency (GHz)	No of passbands	Band width per passband (GHz)	NEAT (K) <sup>1</sup>	Polarisation angle <sup>2</sup>	IFOV (km)
<b>SSM/T-2</b> (Galín <i>et al.</i> , 1993), 1992-2008						
1	183.31±3.0	2	1.0	0.60	H	48 (nadir)
2	183.31±1.0	2	0.5	0.80	H	48 (nadir)
3	183.31±7.0	2	1.5	0.60	H	48 (nadir)
4	91.655±1.25	2	1.5	0.60	H	88 (nadir)
5	150.0±1.25	2	1.5	0.60	H	54 (nadir)
<b>AMSU-B</b> (Robel, 2009), 1998-present						
1	89.0	2	1.0	0.37	V	16.3 (nadir)
2	150.0	2	1.0	0.84	V	16.3 (nadir)
3	183.31±1.00	2	0.5	1.06	V	16.3 (nadir)
4	183.31±3.00	2	1.0	0.70	V	16.3 (nadir)
5	183.31±7.00	2	2.0	0.60	V	16.3 (nadir)
<b>MHS</b> (Robel, 2009), 2005-present						
1	89.0	1	2.4	0.22	V	16.3 (nadir)
2	157.0	1	2.4	0.34	V	16.3 (nadir)
3	183.311±1.0	2	0.5	0.51	H	16.3 (nadir)
4	183.311±3.0	2	0.9	0.40	H	16.3 (nadir)
5	190.311	1	2.2	0.46	V	16.3 (nadir)
<b>ATMS</b> (Weng <i>et al.</i> , 2013) 2011-present						
16	88.2	1	2.0	0.50	V	32.6 (nadir)
17	165.5	1	3.0	0.60	H	16.3 (nadir)
22	183.31±1.0	2	0.5	0.90	H	16.3 (nadir)
20	183.31±3.0	2	1.0	0.80	H	16.3 (nadir)
18	183.31±7.0	2	2.0	0.80	H	16.3 (nadir)
<b>SSMIS</b> (Kunkee <i>et al.</i> , 2008a), 2003-present						
17	91.655	2	1.418 <sup>1</sup>	0.33	V*	12.5 <sup>3</sup>
18	91.655	2	1.411 <sup>1</sup>	0.32	H*	12.5 <sup>3</sup>
8	150	2	1.642 <sup>1</sup>	0.89	H*	12.5 <sup>3</sup>
11	183.31±1	2	0.513 <sup>1</sup>	0.81	H*	12.5 <sup>3</sup>
10	183.31±3	2	1.019 <sup>1</sup>	0.67	H*	12.5 <sup>3</sup>
9	183.31±6.6	2	1.526 <sup>1</sup>	0.97	H*	12.5 <sup>3</sup>
<b>MTVZA-GY</b> (Gorobets <i>et al.</i> , 2007), 2009-present						
25	91.65	2	2.5	0.6	V*	14 x 30
26	91.65	2	2.5	0.6	H*	14 x 30
29	183.31±1.0	2	0.5	0.5	V*	9 x 21
28	183.31±3.0	2	1.0	0.6	V*	9 x 21
27	183.31±7.0	2	1.5	0.8	V*	9 x 21

<sup>1</sup> Values from specification for SSM/T-2, from NOAA-15 for AMSU-B, from NOAA-18 for MHS, from Suomi NPP for ATMS, from DMSP F-16 for SSMIS, and from Meteor-M N2 for MTVZA-GY

<sup>2</sup> The V and H polarizations correspond respectively to electrical fields normal or parallel to the ground track at nadir (rotating by an angle equal to the scan angle for off-nadir directions, except for conical scanners indicated by \*)

<sup>3</sup> Sampling interval along scan direction based on 833km spacecraft altitude

## 2.2 Reanalysis data

Radiative transfer simulations are performed using 6 hourly model grid (TL255L60) data from ERA-Interim, specifically temperature and specific humidity on 60 model levels, surface pressure, land/sea mask, skin temperature, 10-metre eastward and northward wind components, surface geopotential, 2-metre temperature and dewpoint, and sea ice fraction. These fields are interpolated to observation location and then input to the radiative transfer model. Temporal interpolation is not performed; instead, the reanalysis data that are closest in time are used.

In order to assess the stability of SSM/T-2 measurements, temporal consistency of the reanalysis data used as a reference is crucial. Since this cannot be guaranteed, and because there are in fact several known issues with temporal jumps in the representation of the water cycle in ERA-Interim (e.g., Dee *et al.*, 2011), radiative transfer simulations are also performed from another reanalysis, using 3 hourly model grid (TL159L91) data from the ERA-20C control experiment. This reanalysis data were produced assimilating surface observations only and resemble very much those generated by an Ensemble of Data Assimilation (EDA) of 10 members presented by Poli *et al.* (2013), with some minor differences. In addition, JRA-55 data were also used for the period from 31 December 2000, 21 UTC to 8 January 2001, 21 UTC.

In ODB files, the following four fields are interpolated to observation location and added to each observational record: skin temperature, sea ice fraction, elevation (from the surface geopotential) and land/sea mask. Further detail is given in appendix A.

## 3 Radiative transfer calculations

The Radiative Transfer for the TIROS Operational Vertical Sounder (RTTOV) version 11.2 (Saunders *et al.*, 2013) is used to conduct fast radiative transfer calculations. The radiative transfer coefficients for SSM/T-2 were generated and supplied by Peter Rayer from the EUMETSAT Satellite Application Facility on Numerical Weather Prediction (NWP-SAF). Surface emissivities are estimated with the Fast Microwave Emissivity Model (FASTEM)-5 (Liu *et al.*, 2011) over sea, and assumed to be 0.95 over land and 0.90 over sea ice respectively.

Since the emission from the ocean surface is polarised, observed radiances considerably vary with the direction of polarisation especially for surface-sensitive channels. However, the polarisation state of the SSM/T-2 can be qualified as unspecified: some publications assume *vertical* polarisation at nadir (e.g. Felde and Pickle, 1995), while others assume *horizontal* polarisation at nadir (e.g. Wessel and Boucher, 1998). Burns *et al.* (1998) investigated this “unspecified” polarisation state by comparing observations and simulations, and concluded that the antenna was oriented towards horizontal polarisation in the limit of nadir viewing. This result was corroborated by information from the Aerojet system engineer for the SSM/T-2 project (Burns *et al.*, 1998). A comparison between observations and simulations from window channels in **Figure 1** demonstrates that assuming vertical polarisation at nadir results in large scan angle dependent biases that are symmetrical with respect to nadir. However, assuming horizontal polarisation at nadir almost completely removes the scan angle dependent biases. Based on this finding, radiative transfer simulations presented thereafter assume horizontal polarisation at nadir.

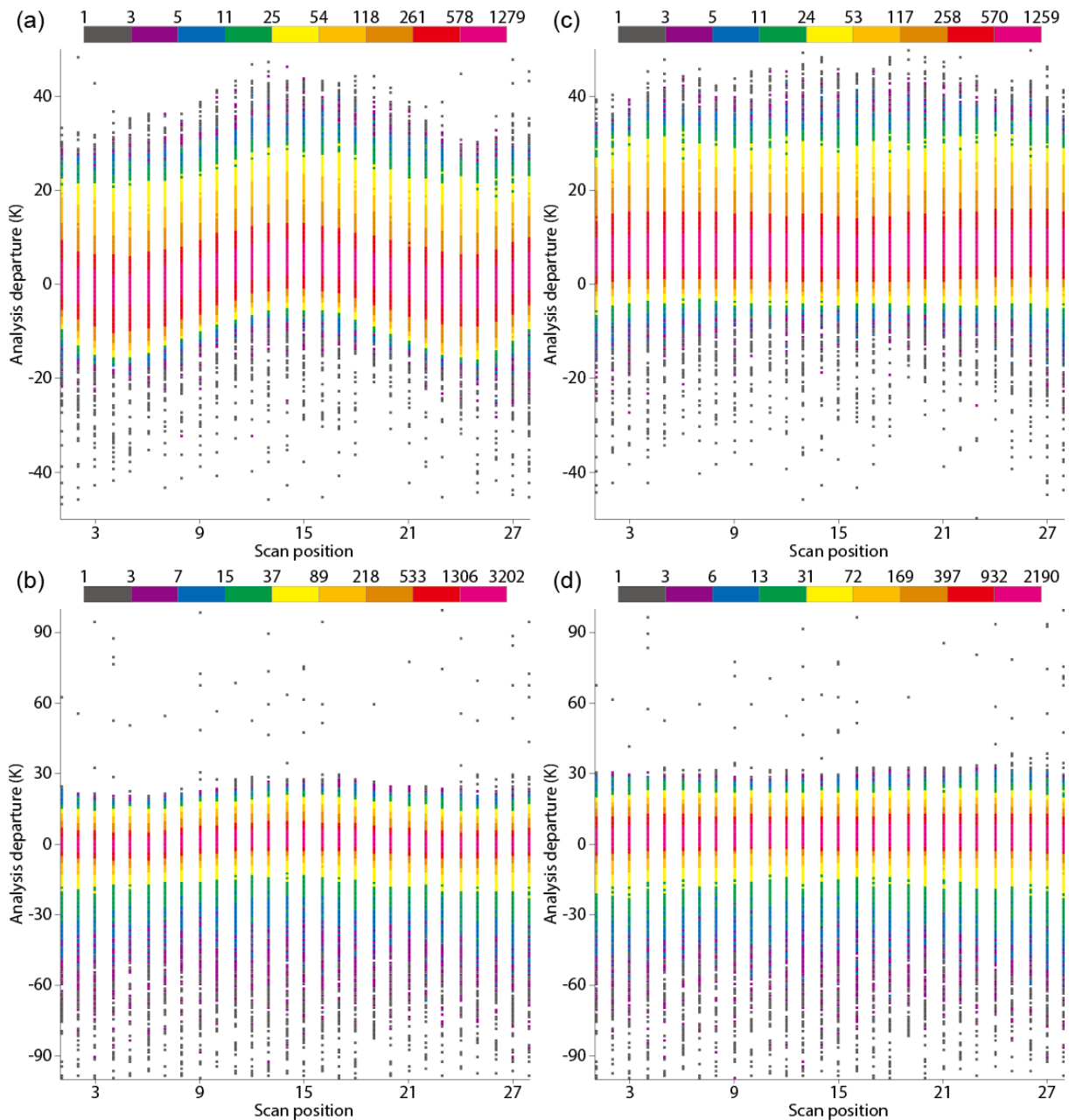


**Figure 1.** Scatter density plots between scan position and analysis departure for (a, c) channel 4 and (b, d) channel 5 of SSM/T-2 on DMSP 12. Polarisation at nadir is assumed to be vertical in (a, b) and horizontal in (c, d). The statistics were computed using the data over sea from 31 December 2000, 21UTC to 8 January 2001, 21 UTC. ERA-Interim profiles were used for the radiative transfer simulations.

Regarding the centre frequency of channel 4, there exist both documents indicating 91.655 GHz (e.g. Galin *et al.*, 1993) and those indicating 91.665 GHz (e.g. Falcone *et al.*, 1992). Since the tropospheric humidity channels (1-3) share a single local oscillator with one of the window channel (4) by using the doubled frequency (183.31 GHz) (Galín *et al.*, 1993), the correct centre frequency of channel 4 should be 91.655 GHz. However, the radiative transfer coefficients used in this study were generated assuming

91.665 GHz, too high by 0.010 GHz. Nevertheless, the impact on the radiative transfer simulations should be minimal because the emission/absorption varies slowly with frequency in this region (Roger Saunders, personal communication).

Since the SSM/T-2 dataset does not contain satellite zenith angles that are necessary for radiative transfer simulations, they are computed from satellite altitudes, nominal nadir angles ( $-40.5+3.0*(\#scan\ position-1)$  (degree)) and the Earth's radius as an ellipsoid of revolution. It should be noted that surface elevation is not taken into account; consequently, satellite zenith angles over high terrain are overestimated.

In ODB files, simulated brightness temperatures and difference between observations and simulations are added to each observational record. Further detail is given in appendix A.

## 4 Results

### 4.1 Geolocation error

Geolocation errors are one of the main sources of uncertainty in satellite microwave observations and have serious effects on inter-calibrating, validating and retrieving geophysical variables from them (Moradi *et al.*, 2013). Since there is a large difference between surface emissivities over land and sea in the microwave frequencies, large geolocation errors lead to erroneous surface emissivities being used in radiative transfer simulations for observations near shorelines and result in distinctive departures of window channels, which have large sensitivities to the surface. **Figure 2** shows departures from the ERA-Interim analysis for channel 4 of SSM/T-2 on each satellite. Among these satellites, DMSP 14 exhibits especially large departures along shorelines with opposite signs in east and west coasts, which is a pattern that emerges when there are roll errors in the spacecraft attitude or sensor mounting for polar orbiting satellites.

Berg *et al.* (2013) corrected geolocation errors in data from the Special Sensor Microwave/Imager (SSM/I) on DMSP satellites using more accurate spacecraft ephemeris and sensor mounting angles estimated from differences between brightness temperatures of ascending and descending orbits to produce FCDRs from these data. A similar correcting method might be applicable to the geolocation errors in SSM/T-2 data.

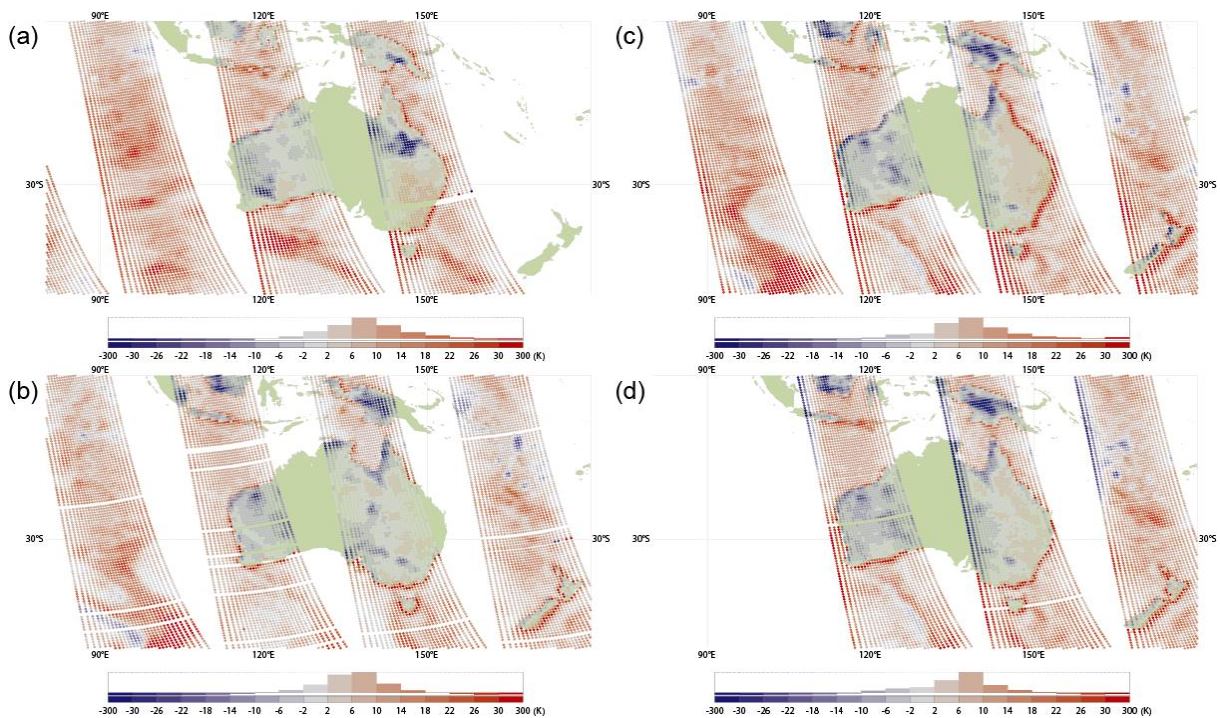


**Figure 2.** Departures from the ERA-Interim analysis for channel 4 of SSM/T-2 on (a) DMSP 11, (b) DMSP 12, (c) DMSP 14 and (d) DMSP 15. The data are for around 3 January 1999, 12 UTC for DMSP 11 and around 3 January 2001, 12 UTC for the others.

## 4.2 Scan angle dependent biases

It is well known that the measurements at several outermost positions on the solar side of the SSM/T-2 were contaminated by the glare obstruction bracket, which was designed to keep sun light out of the instrument cavity (e.g. Miao *et al.*, 2001). **Figure 3** shows scatter density plots between scan position and analysis departure for channel 2 of SSM/T-2 on each satellite. Significant effects of the interference from the glare obstructor can be found in measurements at the scan positions 26 to 28 on all satellites except DMSP 12. These data should be excluded from production of CDRs and use in reanalyses. No similar effect is found for DMSP 12. The cause of this difference, unknown at the moment, should be investigated, and possibly traced to satellite design.

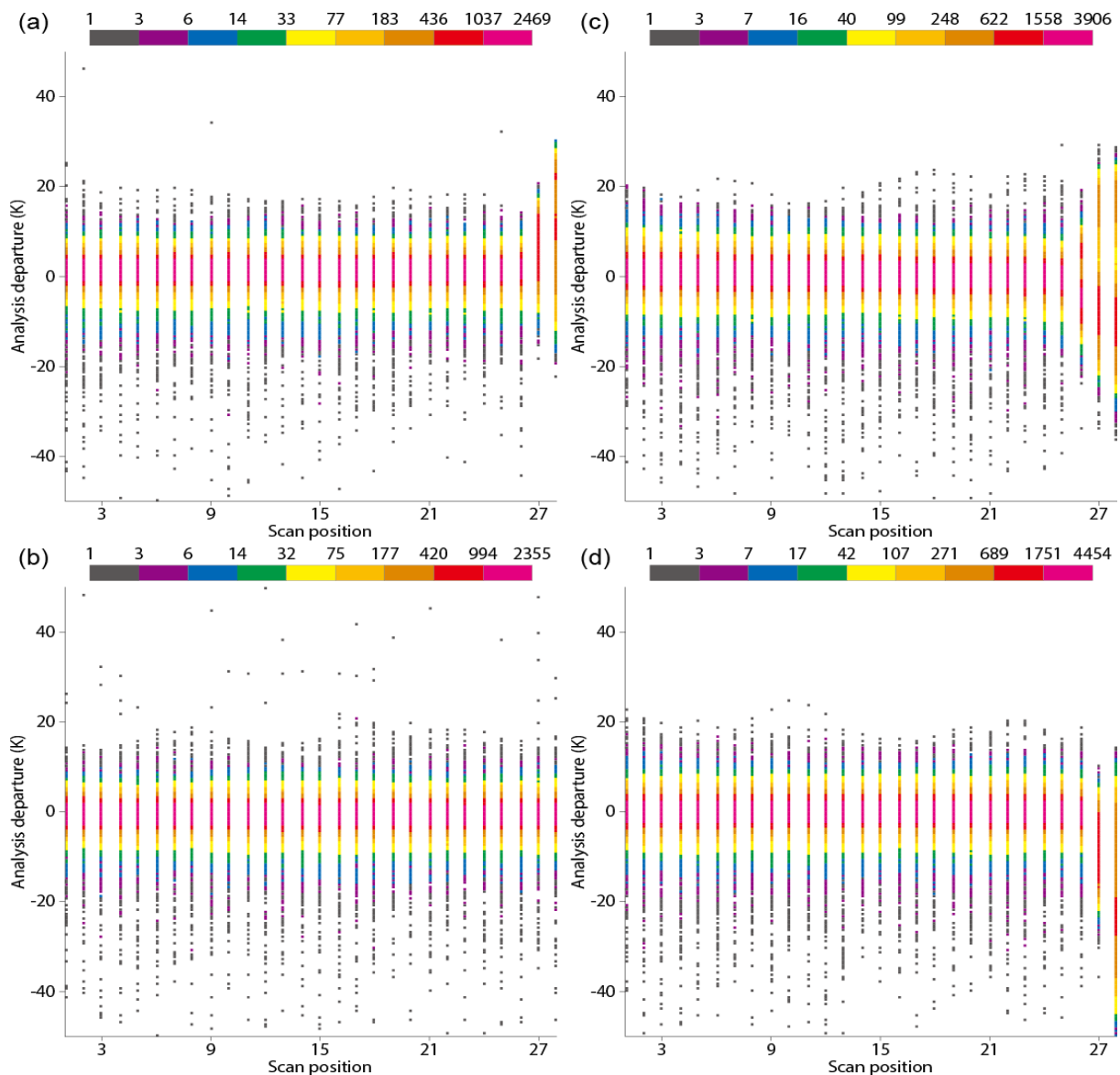


**Figure 3.** Scatter density plots between scan position and analysis departure for channel 2 of SSM/T-2 on (a) DMSP 11, (b) DMSP 12, (c) DMSP 14 and (d) DMSP 15. The statistics were computed using the data over sea from 31 December 1998, 21 UTC to 8 January 1999, 21 UTC for DMSP 11 and from 31 December 2000, 21 UTC to 8 January 2001, 21 UTC for the others. ERA-Interim profiles were used for the radiative transfer simulations.

### 4.3 Poor quality data during the time period before 1994

Departures during the time period before 1994 exhibit a quasi-regular stripe pattern as shown by maps in **Figure 4(a)**. This periodicity is due to the fact that the brightness temperature array in the SSM/T-2 dataset contains a cluster of several corrupted data approximately every 70 elements (though not exactly, this irregularity varies). This array has two dimensions of 28 scan positions by five channels. Thus, a large departure appears every 10 data points or so for each channel. Quality flags in the SSM/T-2 dataset are not always set for these poor quality data (**Figure 4(b)**). Therefore, additional quality control such as departure check is essential to remove them (**Figure 4(c)**).

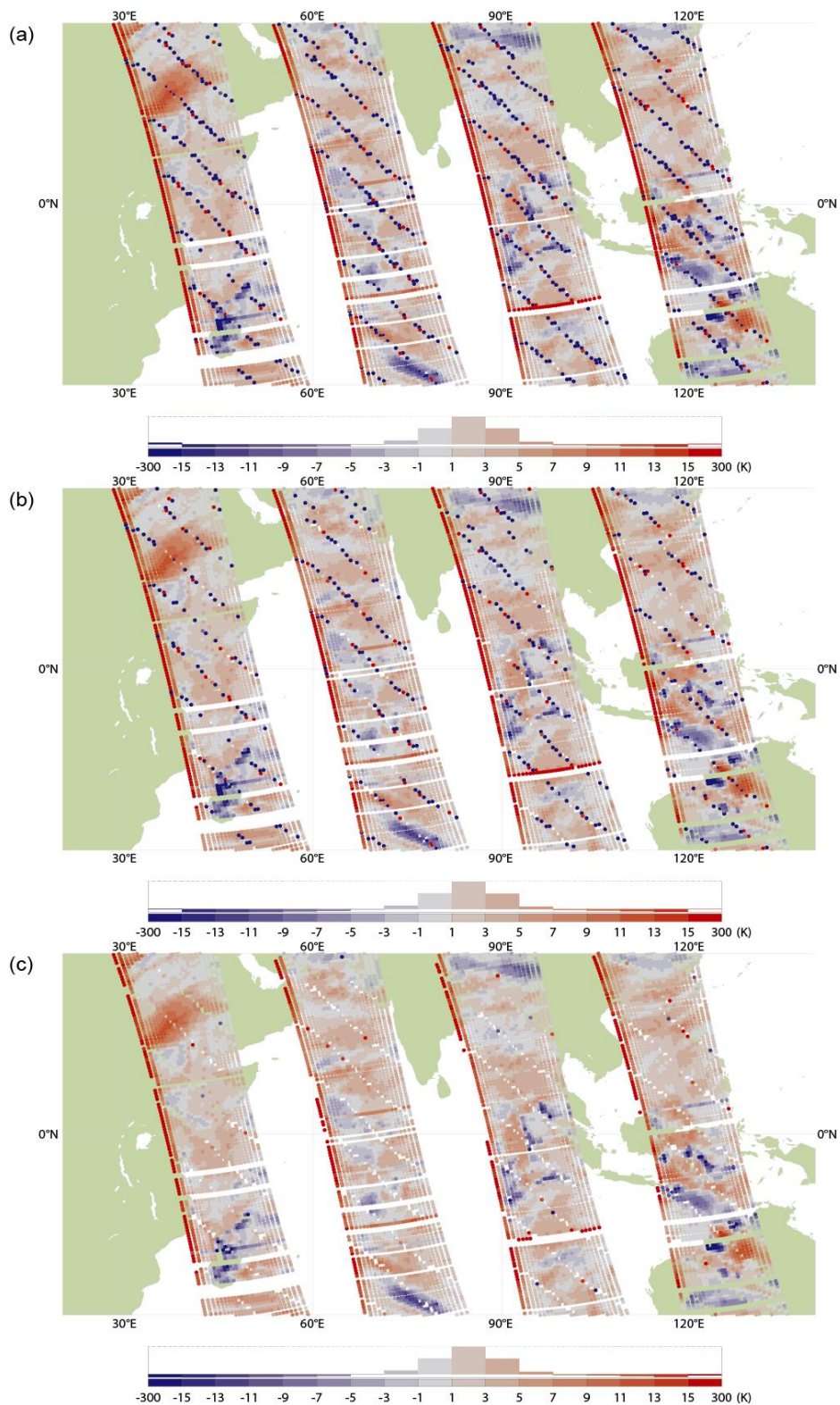


**Figure 4.** Departures from the ERA-Interim analysis for channel 2 of SSM/T-2 on DMSP 11 around 5 January 1993, 12 UTC. (a) All data, (b) those after quality flag check, and (c) those after quality flag check and departure check ( $\pm 20$  K).

#### 4.4 Comparison between observed and simulated brightness temperatures

**Figure 5** shows scatter density plots between observed and simulated brightness temperatures from each channel of SSM/T-2 on DMSP 15 over sea from 31 December 2000, 21 UTC to 8 January 2001, 21 UTC. During this period, radiances from AMSU-B were assimilated in ERA-Interim, and its tropospheric humidity analysis should be reasonably accurate. For DMSP 15, there is no major issue such as geolocation errors during this period. In the plots for tropospheric humidity channels (**Figure 5(a-c)**) and the 150 GHz channel (**Figure 5(e)**), some of the data are distributed off the diagonal on the left due to the fact that the scattering effect of hydrometeors such as cloud particles are not taken into account in the radiative transfer simulations.

To detect cloud-affected measurements, the cloud filtering method of Buehler *et al.* (2007) for AMSU-B is employed in this study. The method uses two criteria: a viewing angle ( $\theta$ ) dependent threshold on the brightness temperature at  $183.31 \pm 1.0$  GHz ( $T_b(183.31 \pm 1.0$  GHz)), and a threshold on difference between the brightness temperature at  $183.31 \pm 3.0$  GHz ( $T_b(183.31 \pm 3.0$  GHz)) and  $T_b(183.31 \pm 1.0$  GHz). The former criterion is based on the fact that  $T_b(183.31 \pm 1.0$  GHz) should be above around 240 K (for nadir looking measurements) in clear skies. In this study, we derived a regression equation from the values for AMSU-B (Buehler *et al.*, 2007, Table 1), and then estimated a threshold for each viewing angle ( $\theta$ ) of SSM/T-2. The latter criterion is derived from the fact that  $T_b(183.31 \pm 1.0$  GHz) is colder than  $T_b(183.31 \pm 3.0$  GHz) in clear skies due to the atmospheric temperature lapse rate, whereas  $T_b(183.31 \pm 1.0$  GHz) can be warmer than  $T_b(183.31 \pm 3.0$  GHz) in the presence of ice clouds. Specifically, measurements satisfying either of the following criteria are considered affected by clouds in this study.

$$T_b(183.31 \pm 1.0 \text{ GHz}) \leq 252.49 - 12.395 / \cos(\theta) \quad (1)$$

$$T_b(183.31 \pm 3.0 \text{ GHz}) - T_b(183.31 \pm 1.0 \text{ GHz}) \leq 0.0 \quad (2)$$

**Figure 6** shows the same scatter density plots as **Figure 5** except that cloud-affected measurements, according to the test explained above, are excluded. The data that pass the cloud filtering are in general distributed along the diagonal. However, the distribution tends to be biased slightly to the left in the middle part for the lower tropospheric humidity channel (**Figure 6(c)**) and in the upper part for the 150 GHz channel (**Figure 6(e)**). Those measurements are most likely the ones affected by cloud particles or rain drops in the lower troposphere because the cloud filtering method of Buehler *et al.* (2007) is designed primarily for ice clouds in the upper troposphere. It can also be seen that simulated brightness temperatures for window channels are considerably lower than observations, indicating that radiances from the surface are underestimated in the radiative transfer simulations. For the lower tropospheric humidity channel (**Figure 6(c)**), the distribution exhibits different biases in the lower part and above. The data in the lower part mainly represent observations in dry regions where they have substantial sensitivity to the surface. Therefore, the colder simulations for those observations are most likely due to the same cause as in the window channels.

Simmons *et al.* (2014) pointed out a moist bias in the tropical upper troposphere in the ERA-Interim background. The moist bias is confirmed in **Figure 5(b)** and **Figure 6(b)**, where the centre of distribution is located slightly off the diagonal to the right, meaning that simulations are colder except in the lower part of the distribution. When the measurements are compared with simulations using the JRA-55 profiles, the centre of distribution is located slightly off the diagonal to the left (**Figure 7(b)**), which is

the opposite to the case of ERA-Interim. This is due to the fact that the forecast model used for JRA-55 has a dry bias in the upper and mid troposphere (Kobayashi *et al.*, 2015). Thus, average departures themselves depend on the biases of the reanalyses used as references.

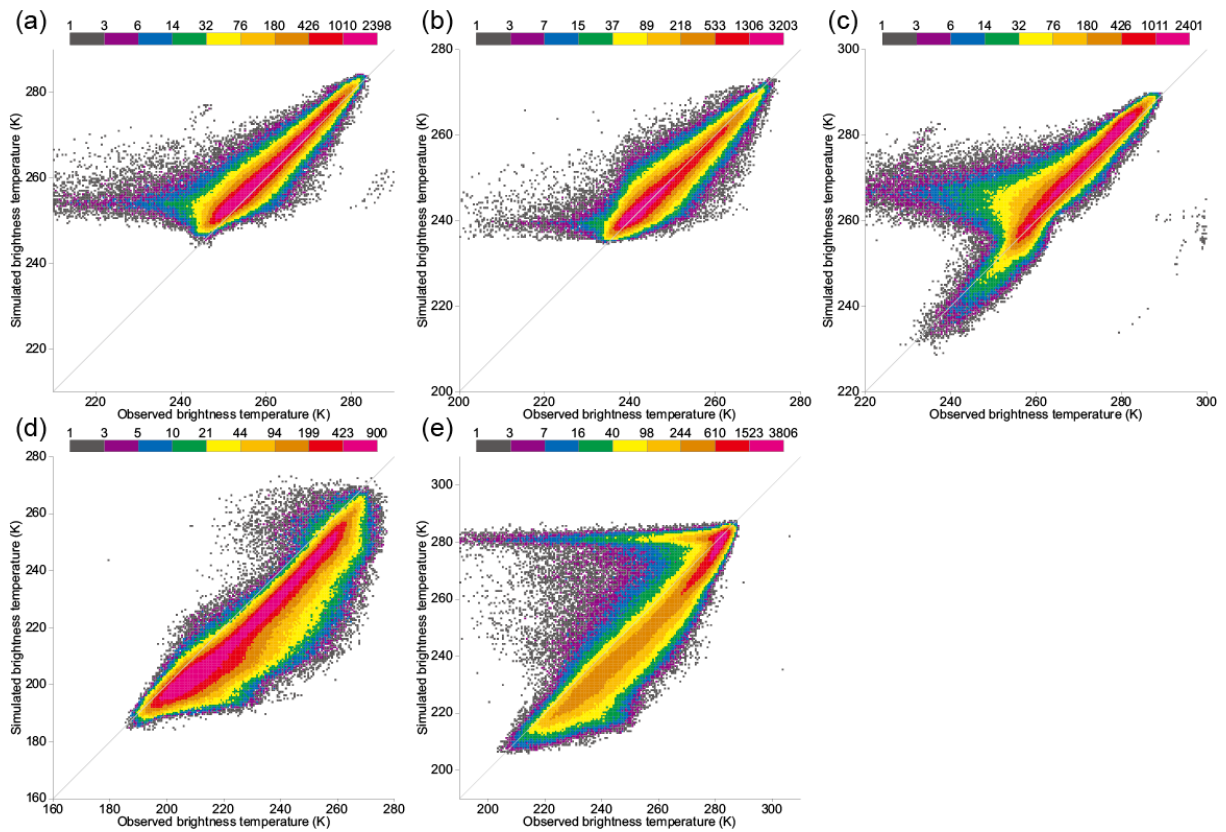


**Figure 5.** Scatter density plots between observed and simulated brightness temperatures from (a) channel 1, (b) channel 2, (c) channel 3, (d) channel 4 and (e) channel 5 of SSM/T-2 on DMSP 15 over sea from 31 December 2000, 21 UTC to 8 January 2001, 21 UTC before cloud filtering. ERA-Interim profiles were used for the radiative transfer simulations.

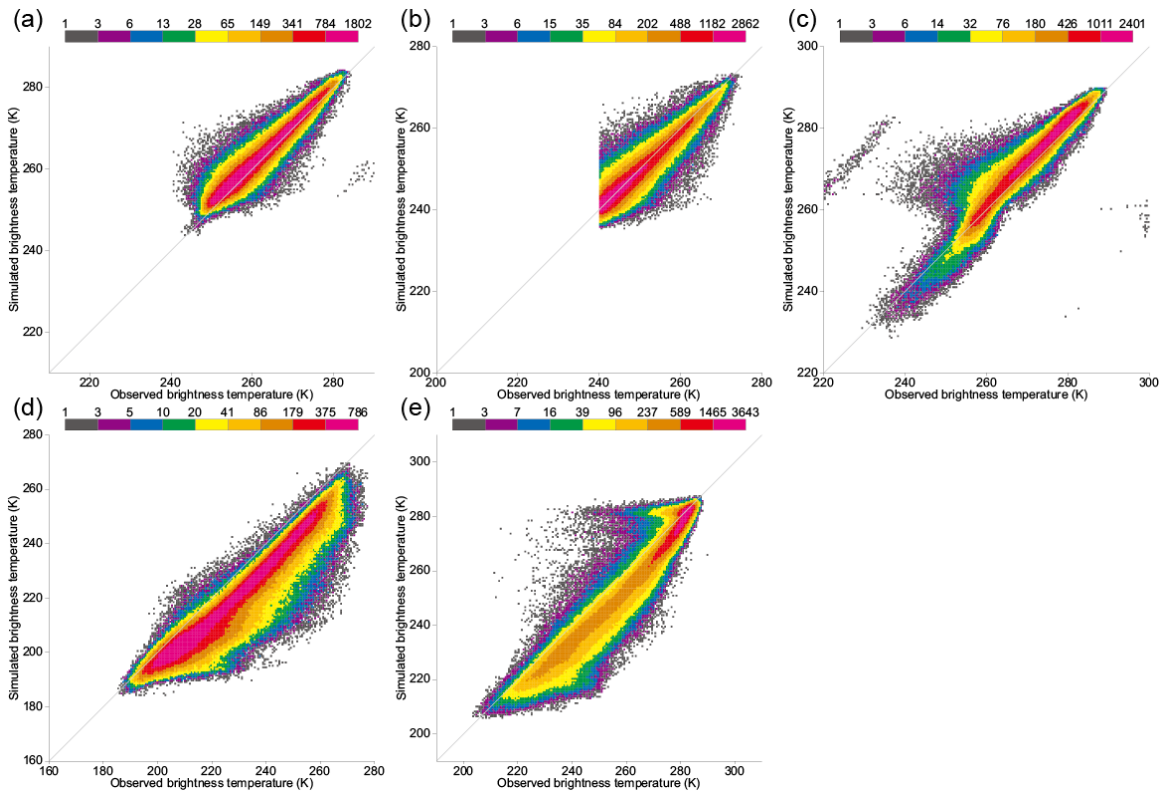


Figure 6. As Figure 5, but after cloud filtering.

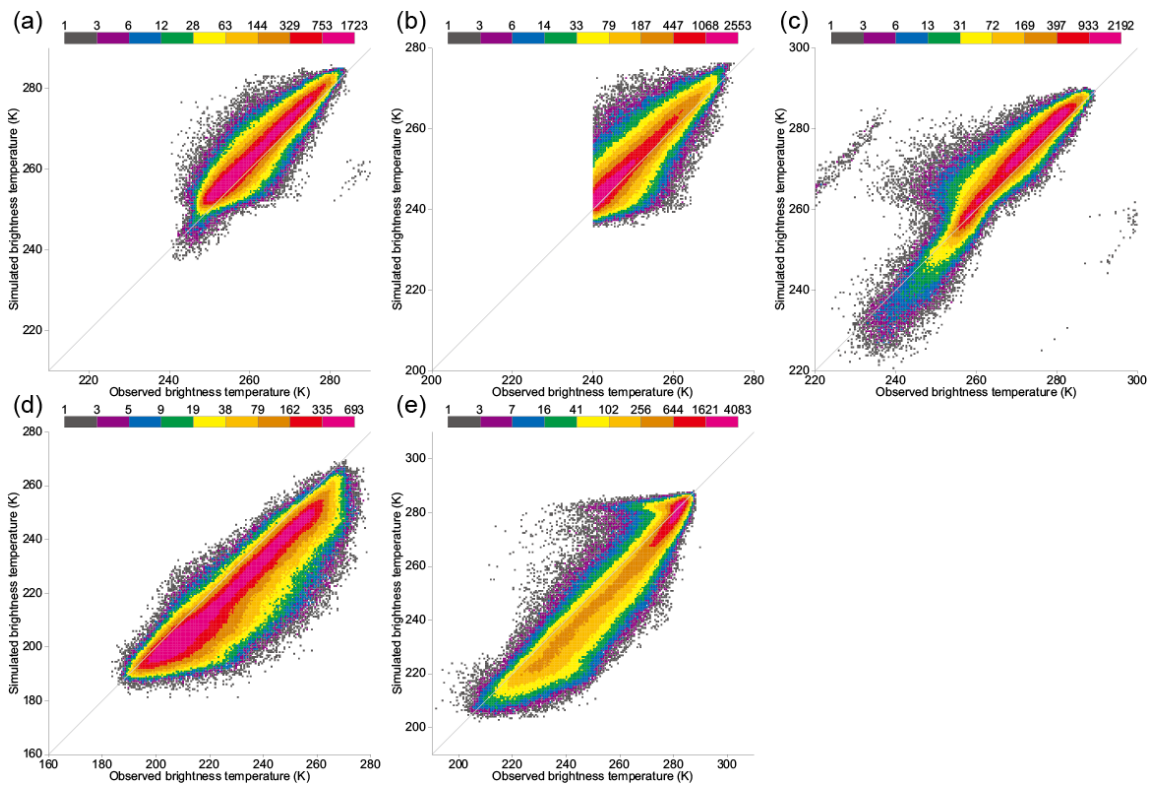


Figure 7. As Figure 6, but for simulations using JRA-55 profiles.

The following subsection focuses the assessment on the stability of biases and inter-satellite biases.

#### 4.5 Stability of SSM/T-2 measurements

**Figures 8 to 12** show monthly time series for the departures from the ERA-Interim analysis over the tropical ocean for the upper, mid and lower tropospheric humidity channels, and the 150 GHz and 91.655 GHz window channels (channels 2, 1, 3, 5 and 4, respectively). **Figure 13** shows 12-month running mean brightness temperatures from SSM/T-2 over the tropical ocean and radiative transfer simulations using ERA-Interim profiles; **Figure 14** does the same but for radiative transfer simulations using ERA-20C profiles.

##### 4.5.1 Upper tropospheric humidity channel (2)

For DMSP 11, monthly mean departures from the ERA-Interim analysis towards the end of the data record are about 0.5 K smaller than in the beginning (**Figure 8(a)**). Monthly mean departures of DMSP 12 and 14 are in general stable except that they show a sharp drop of about 0.5 K at the end of 2000. It can be seen in time series for average brightness temperatures (**Figure 13(a)**) that simulations using ERA-Interim profiles rise suddenly by 0.5 K around that time; this coincides with the first assimilation of brightness temperatures from AMSU-B in October 2000 (Poli, 2010). On the other hand, we observe no comparable variation at that time in either observations or simulations using ERA-20C profiles (**Figure 14(a)**); ERA-20C was produced assimilating only surface observations. Therefore, the sharp drop around end of 2000 is most likely due to the introduction of AMSU-B to ERA-Interim, thereby constraining better the moist bias therein in the tropical upper troposphere. For DMSP 15, monthly mean departures rise suddenly again by 0.5 K in the year 2003. Thereafter they exhibit an increasing trend, which is not seen in the other satellites. It should be noted that standard deviations of DMSP 14 increase after the year 2001 (**Figure 8(b)**).

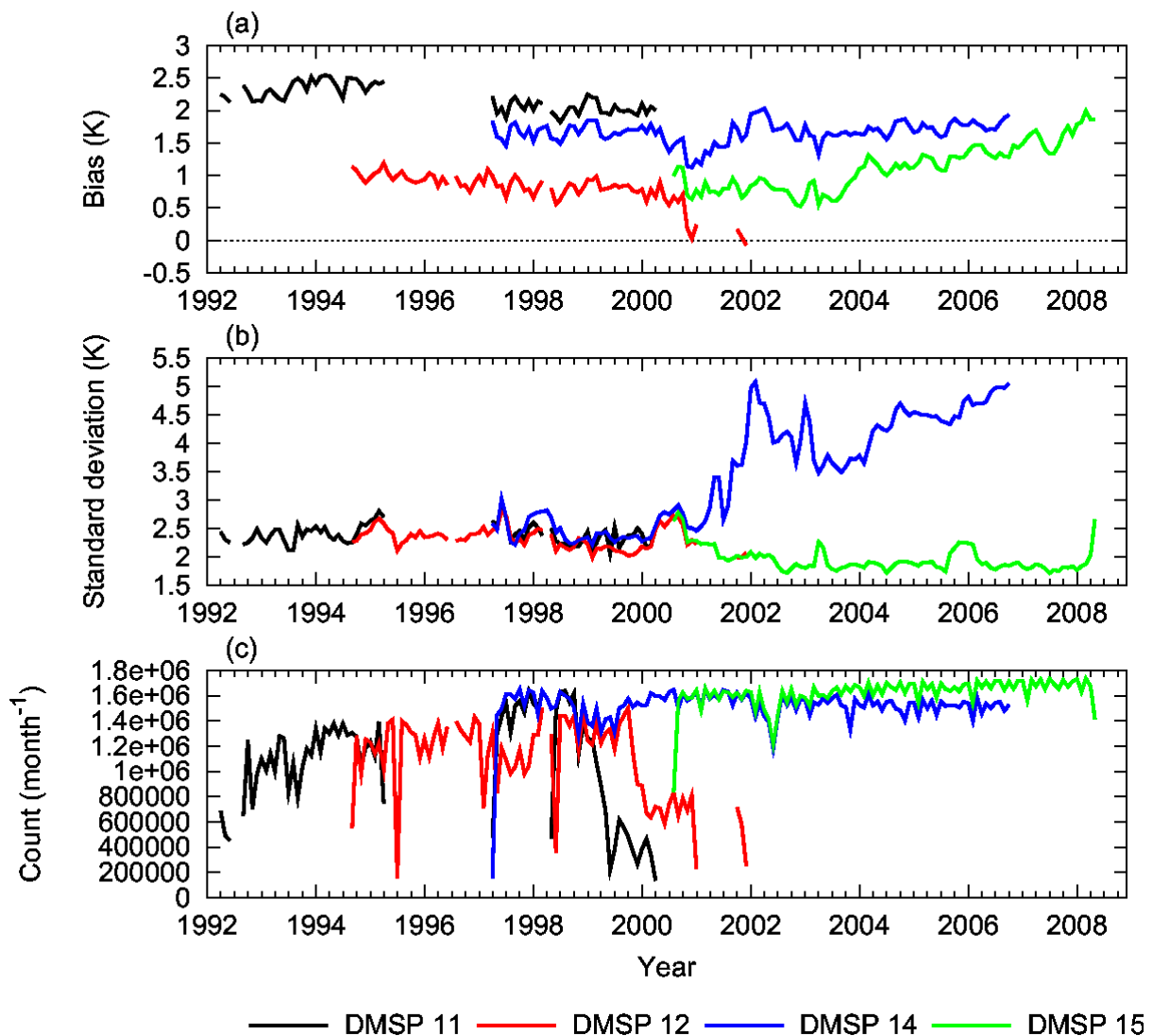


**Figure 8.** (a) Monthly mean and (b) standard deviation of departures from the ERA-Interim analysis, and (c) monthly counts for the upper tropospheric humidity channel (2) over the tropical ocean (30°N to 30°S). The statistics were computed using clear-sky data only.

DMSP 12 and 14 collected observations at almost the same local time (around 20:50) in mid-1999. During this orbital overlapping period, the representation of the diurnal cycle in the validating reanalyses has little impact on estimation of inter-satellite biases. There is a steady difference of about 1 K between departures of DMSP 12 and 14 including in the orbital overlapping period, which suggests a continuous inter-satellite bias between these two satellites. Using the transformation method of Buehler and John (2005) for the upper tropospheric humidity channel (2), the difference of 1 K in brightness temperature should correspond to a difference of around 2 % in relative humidity. Since this magnitude exceeds inter-annual variations, it is essential to correct for such inter-satellite biases before using these data directly in climate applications.

## 4.5.2 Mid tropospheric humidity channel (1)

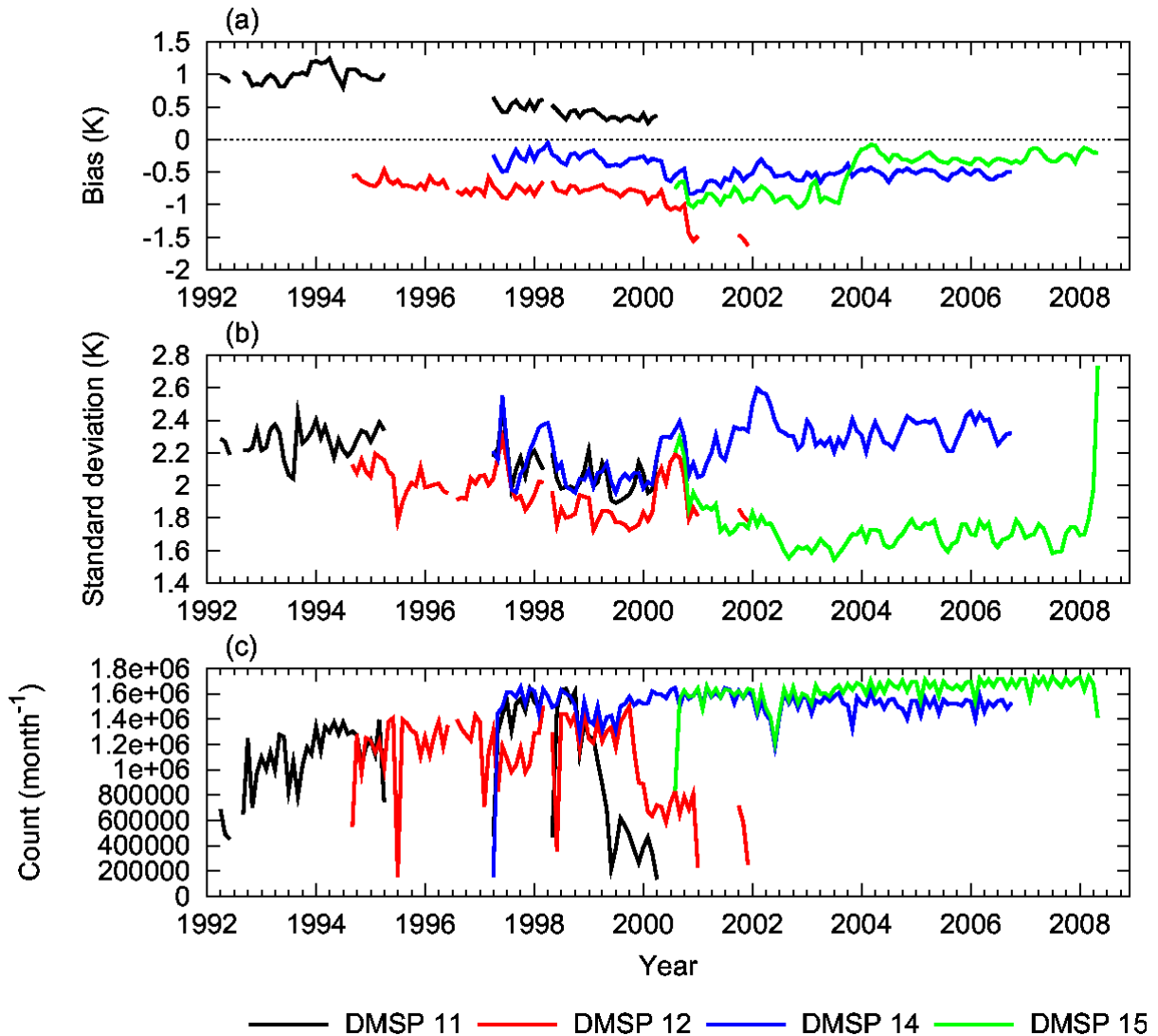


Figure 9. As Figure 8, but for the mid tropospheric humidity channel (1).

Similarly to the upper tropospheric humidity channel (2), it can be seen in **Figure 9(a)** that monthly mean departures of DMSP 11 are about 0.5 K smaller in the second half of the record as compared to the first half; there is a continuous inter-satellite bias of about 0.5 K between DMSP 12 and 14; DMSP 15 exhibits a sudden increase of about 0.5 K in the year 2003. It should be noted that there is a difference of about 0.5 K between brightness temperatures simulated from ERA-Interim for DMSP 12 and 14 (**Figure 13(b)**), which in theory should agree with each other during the orbital overlapping period in mid-1999. This indicates that there is a difference between cloud detection rates of these two satellites, most likely due to inter-satellite biases in the mid and upper tropospheric humidity channels (1, 2), which

are used for the cloud filtering. This suggests that it is important to correct for such inter-satellite biases in order to maintain consistency of cloud filtering across multiple satellites.

4.5.3 Lower tropospheric humidity channel (3)

**Figure 10** shows features similar to those of the mid tropospheric humidity channel (1). In addition, there is a spike in monthly mean departures of DMSP 15 from February to March 2003. Thereafter, they exhibit an increasing trend, which is not seen in any other satellite.

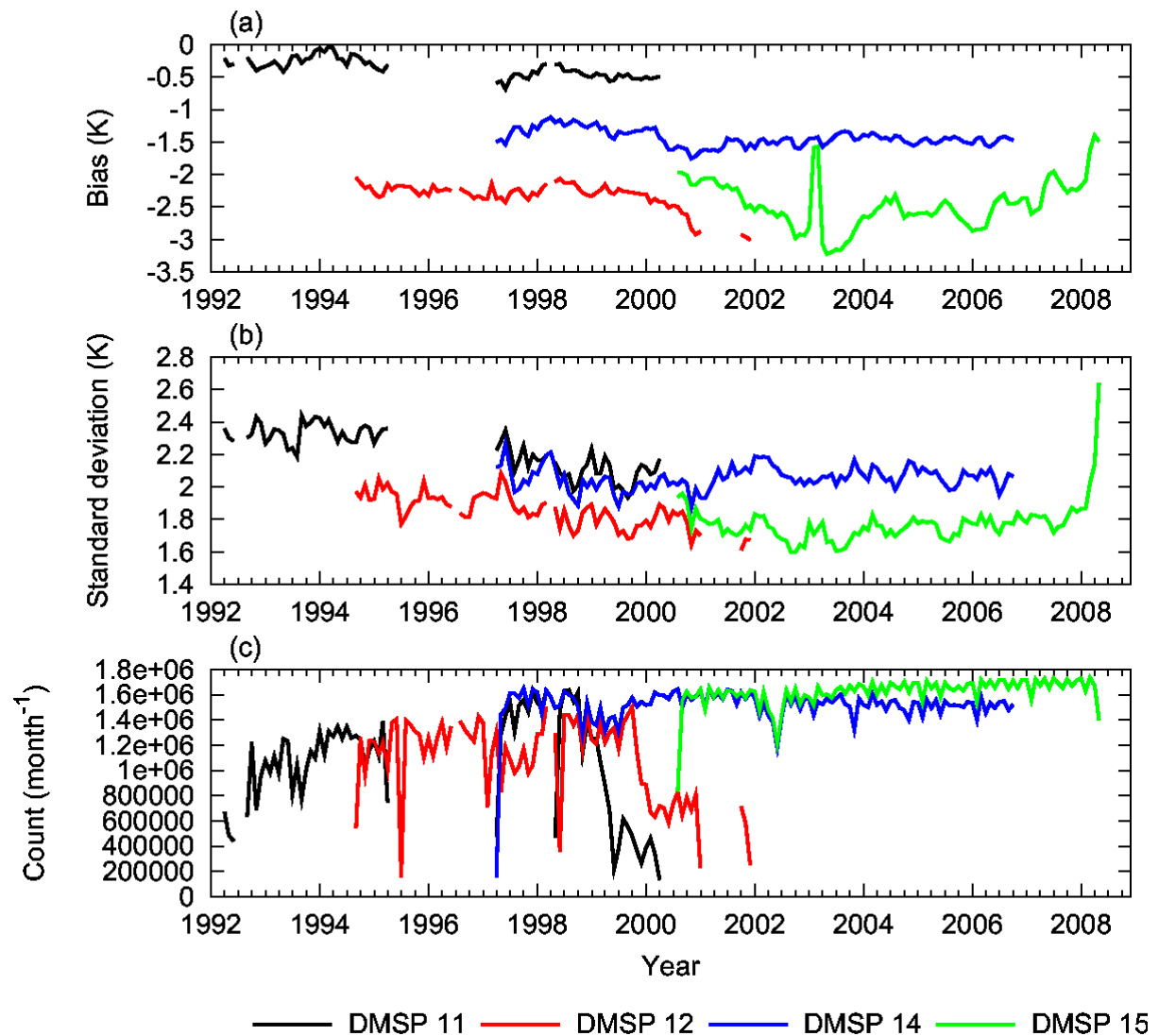


**Figure 10.** As **Figure 8**, but for the lower tropospheric humidity channel (3).

4.5.4 150 GHz channel (5)

Measurements from DMSP 11 became unusable since 20 June 1993, most likely due to failure of the 75 GHz Gunn diode oscillator (Kieu *et al.*, 1994). Measurements from DMSP 15 became unstable since November 2001 (Chung and John, 2013). These measurements are excluded from the statistics shown in **Figure 11**. In addition, DMSP 14 exhibits increase of standard deviations after 1999. After excluding these data, stable measurements are only available for a limited period, which renders them unsuitable for long-term climate monitoring.

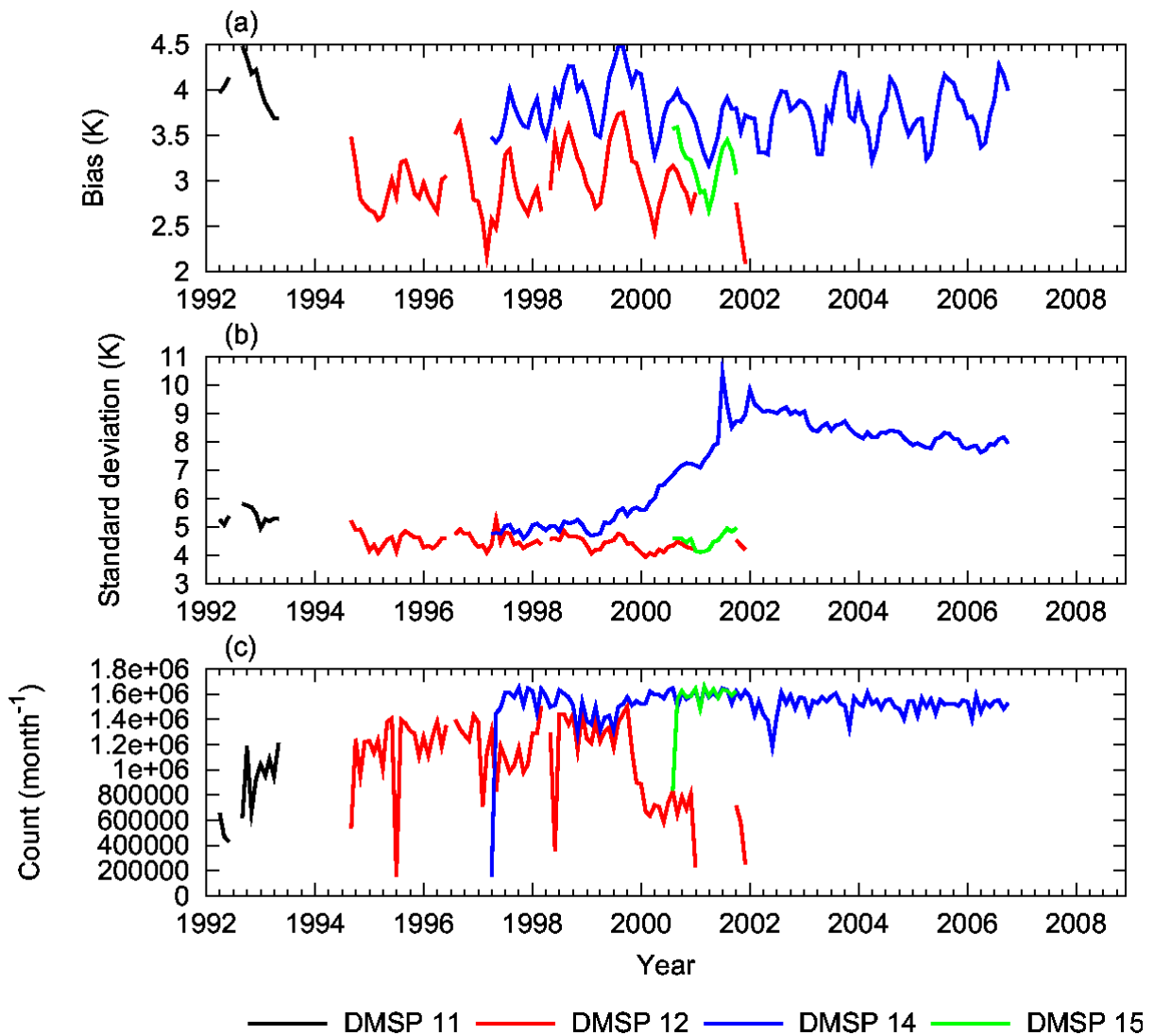


**Figure 11.** As **Figure 8**, but for the 150 GHz channel (5).

#### 4.5.5 91.655 GHz channel (4)

Monthly mean departures from the ERA-Interim analysis in general show increasing trends except DMSP 15, which exhibits a decreasing trend (**Figure 12**). It can also be seen that monthly mean departures of both DMSP 12 and 14 fall by about 0.5 K and standard deviations decrease by about 0.5 K early in 2000. This change comes from a sudden increase in brightness temperatures simulated from ERA-Interim profiles (**Figure 13(e)**), which in turn most likely due to a sudden increase in sea surface temperatures (SSTs) used for ERA-Interim (January 1989-June 2001: National Center for Environmental Prediction (NCEP) 2-Dimensional Variational SST, July 2001-December 2001: NOAA Optimum Interpolation SST v2, January 2002-January 2009: NCEP Real-Time Global SST: Dee *et al.*, 2011). It should be noted that measurements from DMSP 15 were degraded since 14 August 2006 due to interference from a radar calibration beacon ([http://nsidc.org/data/docs/daac/f15\\_platform.gd.html](http://nsidc.org/data/docs/daac/f15_platform.gd.html)), which also affected the SSM/I instrument on the same platform (Hilburn and Wentz, 2008). For this reason, the SSM/T-2 measurements from DMSP 15 are excluded from the statistics after this date.

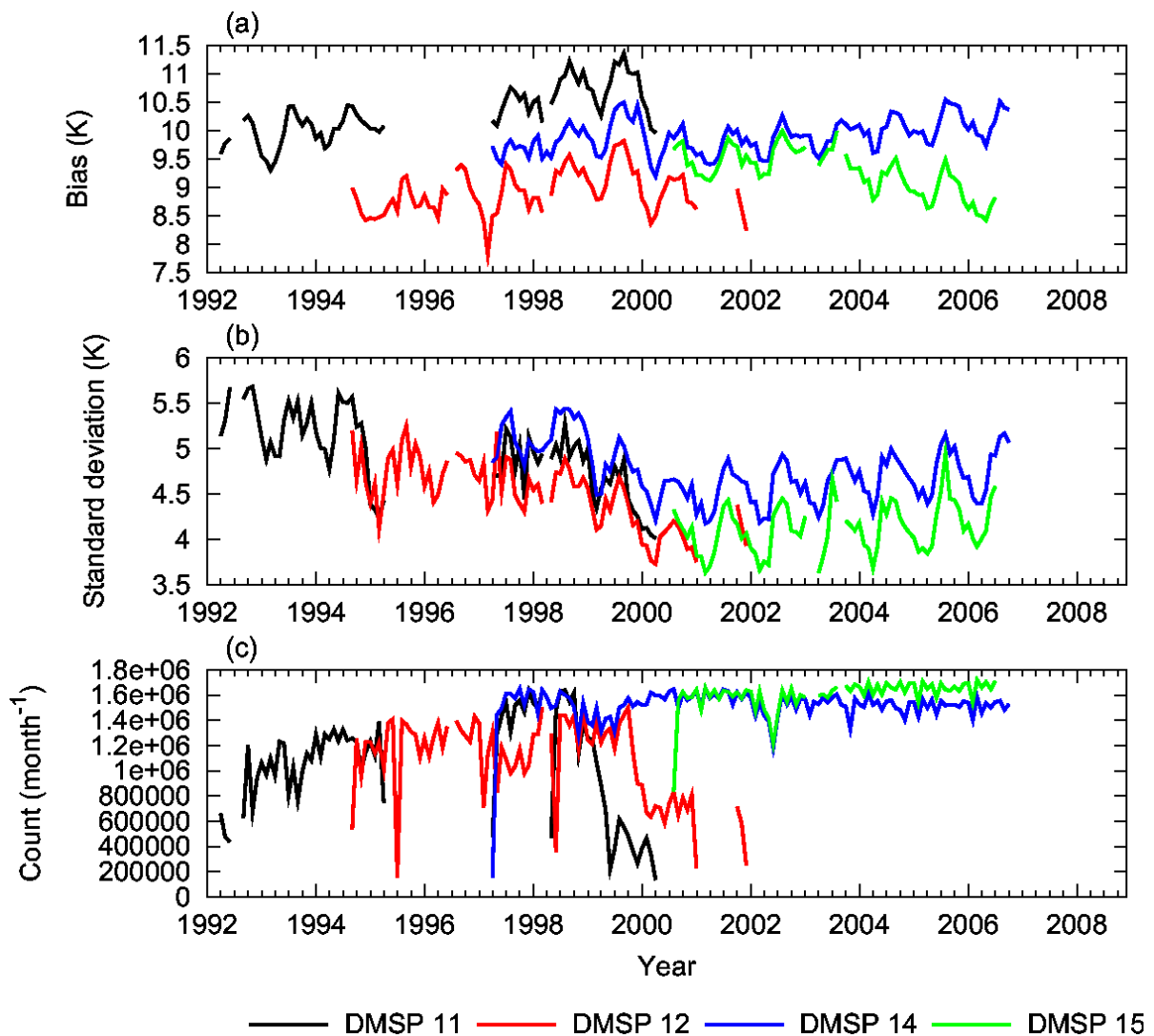


**Figure 12.** As **Figure 8**, but for the 91.655 GHz channel (4).

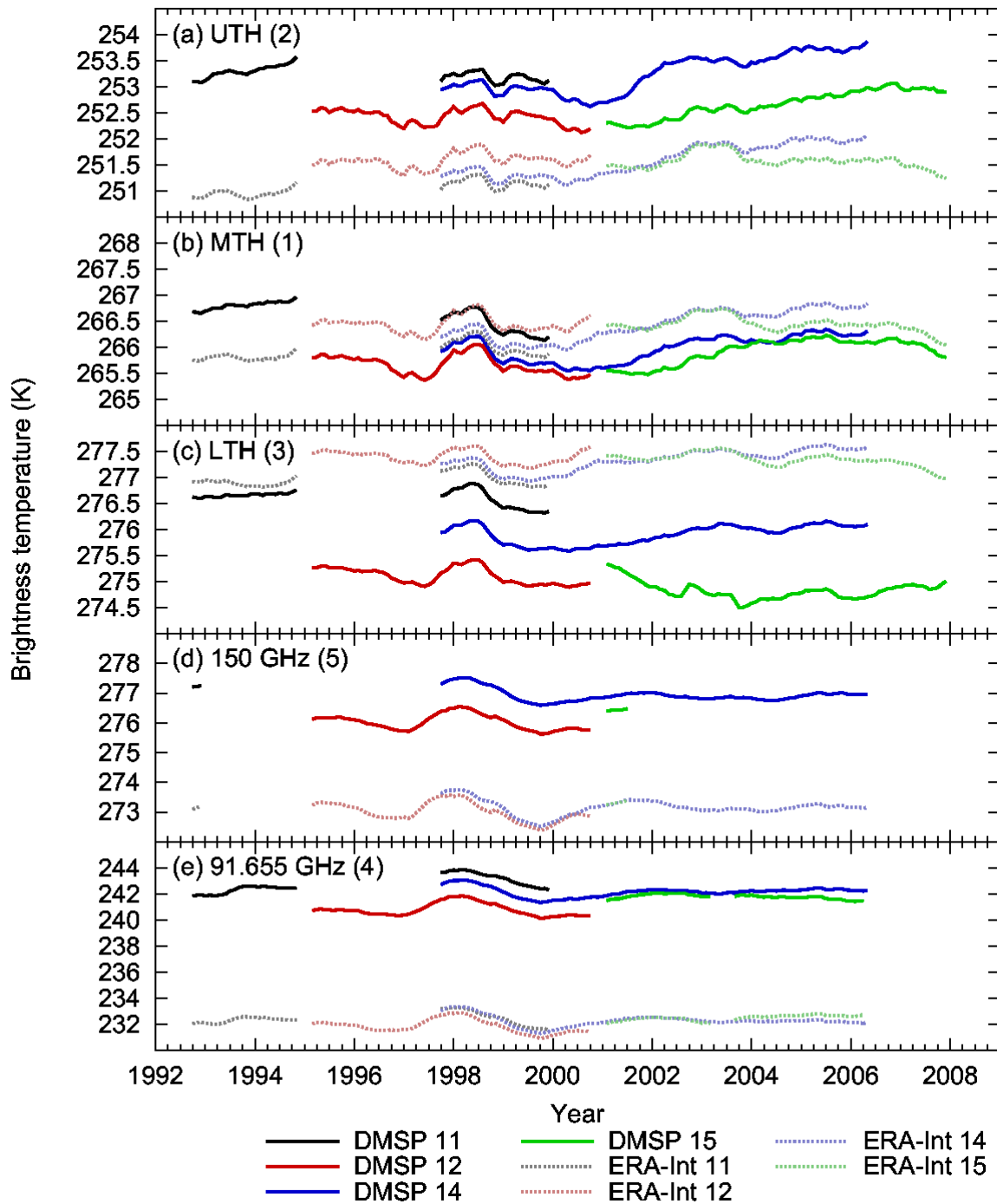


**Figure 13.** 12-month running mean brightness temperatures from SSM/T-2 and radiative transfer simulations using ERA-Interim profiles averaged over the tropical ocean (30°N to 30°S). The statistics were computed using clear-sky data only.

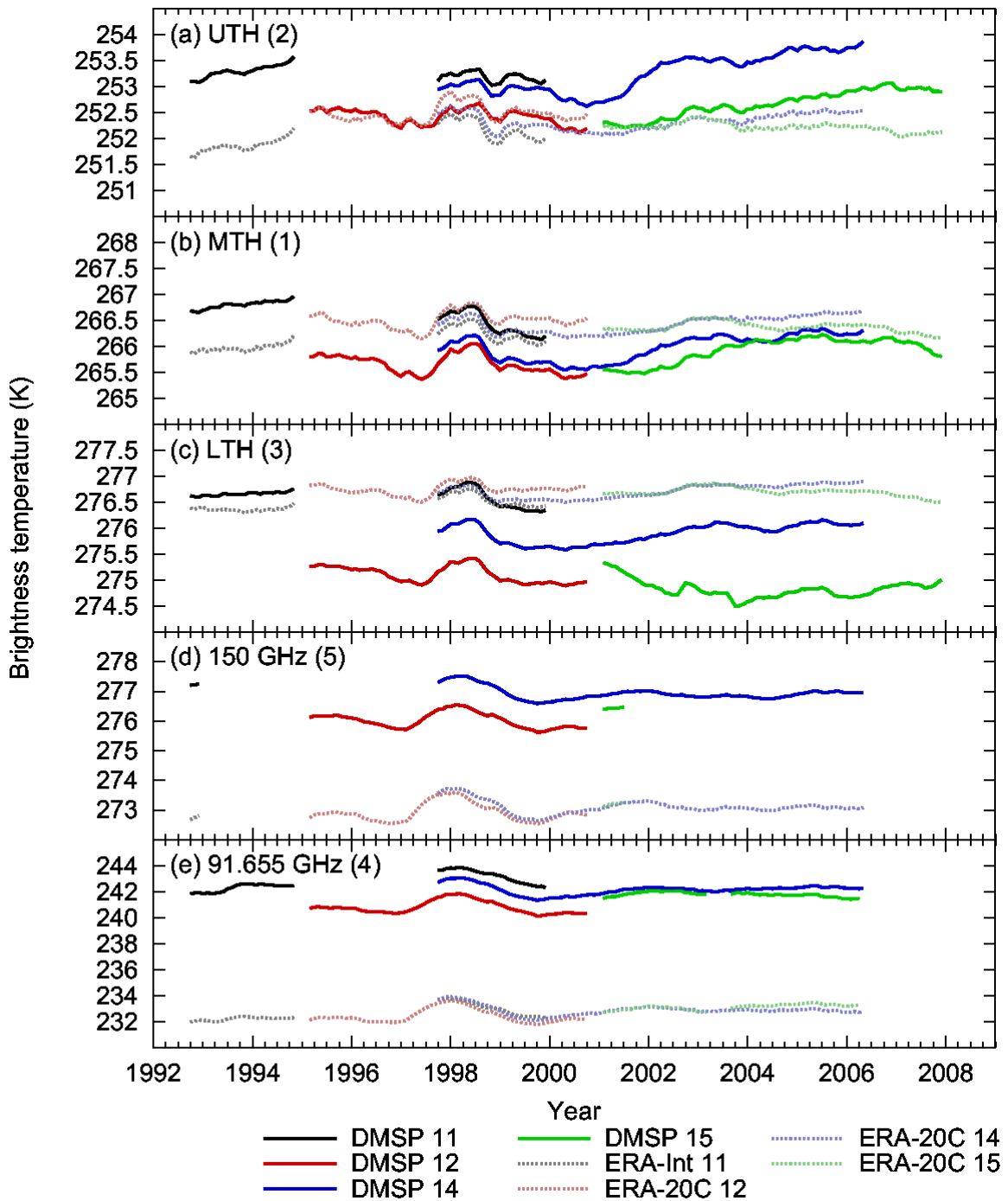


Figure 14. As Figure 13, but for SSM/T-2 and radiative transfer simulations using ERA-20C profiles.

## 5 Second iteration: new computations

After the completion of the computations presented in previous sections, it was found that temperature and humidity fields given to the radiative transfer model were inadvertently shifted by one level downward. This bug had the effect of lowering radiative transfer estimates, and was most likely related to the large biases seen in window channels. In addition, it was also found that there was a bug in the implementation of the cloud filtering criterion (equation (1)) where the threshold for the nadir viewing FOV was applied to all the other FOVs, which resulted in too strict cloud filtering. Since reliable statistical information on error characteristics is essential for producing high quality FCDRs, the entire computations were re-run with a radiative transfer simulation suite revised as follows:

- 1) correction of the bug that temperature and humidity fields given to the radiative transfer model were shifted by one level downward,
- 2) use of proper satellite azimuth angles (the first computations assume azimuth angles of 0 degree),
- 3) use of revised RTTOV coefficients (the centre frequencies are corrected from  $91.665\pm 0.75$  GHz to  $91.655\pm 1.25$  GHz for channel 4 and from  $150.0\pm 0.75$  GHz to  $150.0\pm 1.25$  GHz for channel 5), and
- 4) correction of the bug in the implementation of the cloud filtering criterion (equation (1)) where the threshold for the nadir viewing FOV was applied to all the other FOVs.

**Figure 15** shows the same scatter density plots as **Figure 5**, but for the second computations before cloud filtering. The distribution in **Figure 15** is shifted slightly upward compared with that in **Figure 5**, indicating that simulated brightness temperatures are generally larger than before, mostly due to correction 1 in the list above. In particular, simulated brightness temperatures for window channels 4 and 5 in **Figure 15**(d, e) are larger by about 3 K than in the first computations in **Figure 5**(d, e), resulting in a bias reduction of the same magnitude. Moreover, standard deviations for the lower tropospheric humidity channel (3) and the 150 GHz channel (5) are reduced by about 3%, which can be confirmed from the smaller variations in the scatter density plots.

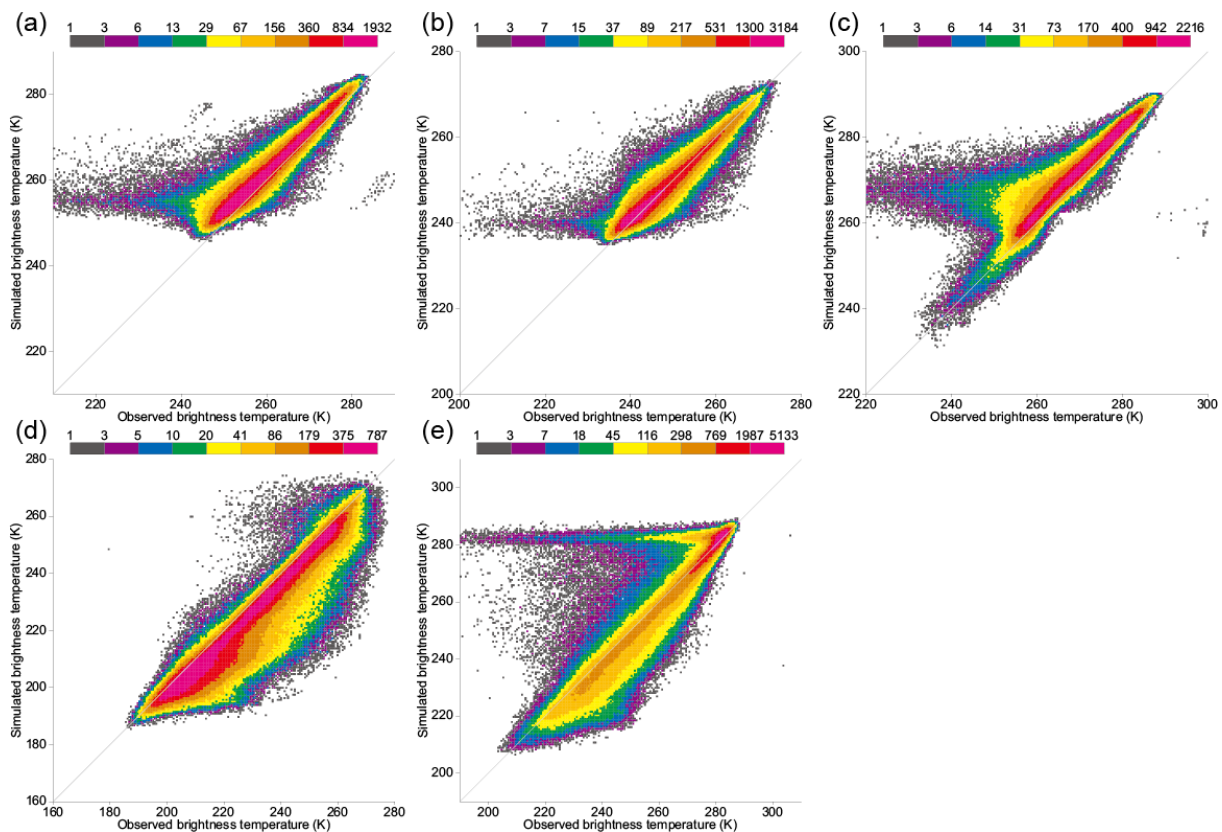


**Figure 15.** As **Figure 5**, but for the period from 31 December 2000, 21 UTC to 7 January 2001, 21 UTC from the second computations before cloud filtering.

**Figure 16** shows the same scatter density plots as **Figure 6**, but for the second computations after cloud filtering. As is evident from the comparison between **Figure 6(b)** and **Figure 16(b)**, some of the data in the first computations were falsely considered affected by clouds due to the bug in the implementation of the cloud filtering criterion. The detection rate in the first computations is about 15 %, whereas it is down to about 9 % in the second computations.

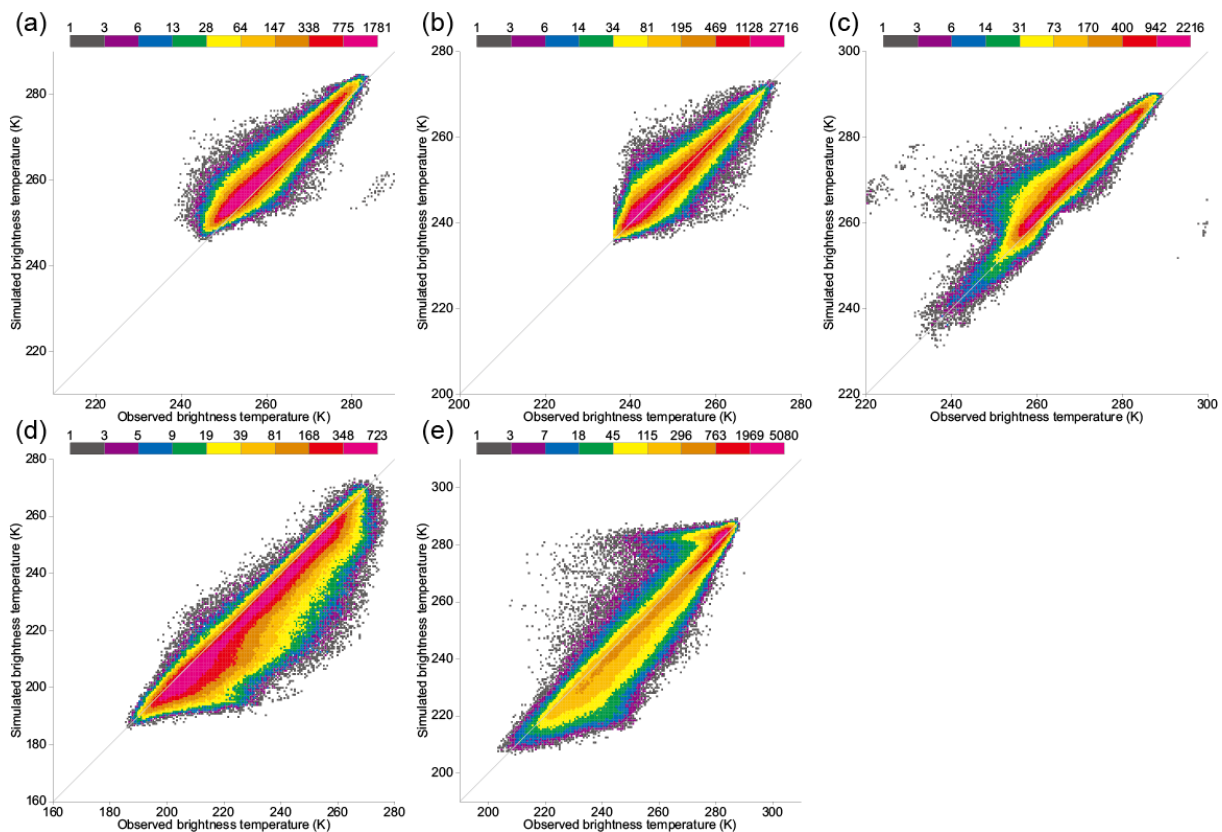


**Figure 16.** As **Figure 6**, but for the period from 31 December 2000, 21 UTC to 7 January 2001, 21 UTC from the second computations after cloud filtering.

**Figures 17 and 18** show the same time series for departures for the 150 GHz and 91.655 GHz channels (5, 4) as **Figures 11 and 12** respectively, but for the second computations. The large positive biases seen in the first computations for the window channels are reduced significantly in the second computations. For the 150 GHz channel (**Figure 17**) in particular, departures generally remain within  $\pm 1$  K and standard deviations have slightly decreased compared with the first computations. On the other hand, the 91.655 GHz channel still exhibits a large positive bias of around 5 K, which indicates that radiances from the surface are underestimated in the radiative transfer simulations.

Inter-satellite biases estimated from the second computations are almost the same as those from the first computations. It is essential to correct for inter-satellite biases before using these data directly in climate applications.

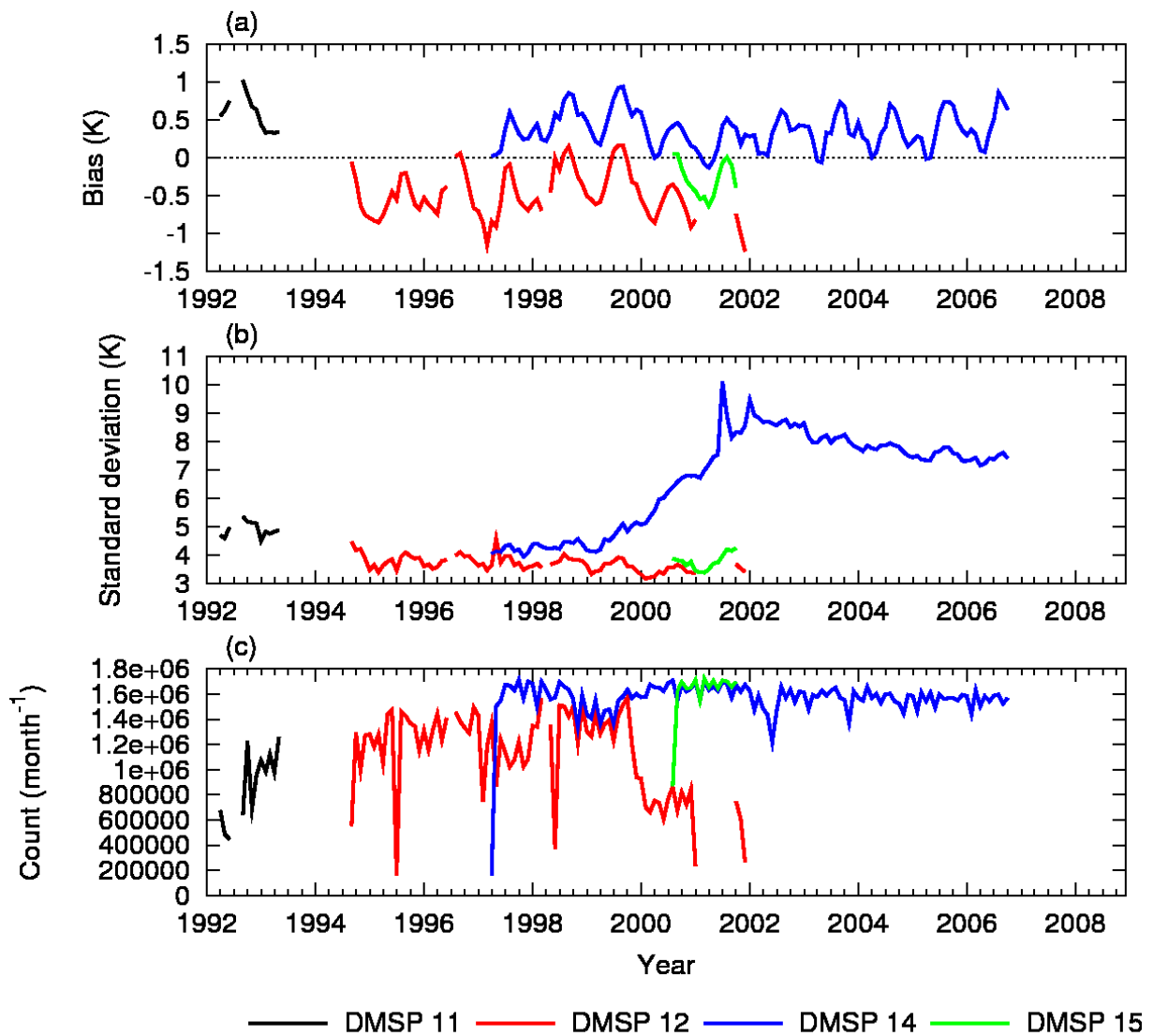


Figure 17. As Figure 11, but for the second computations.

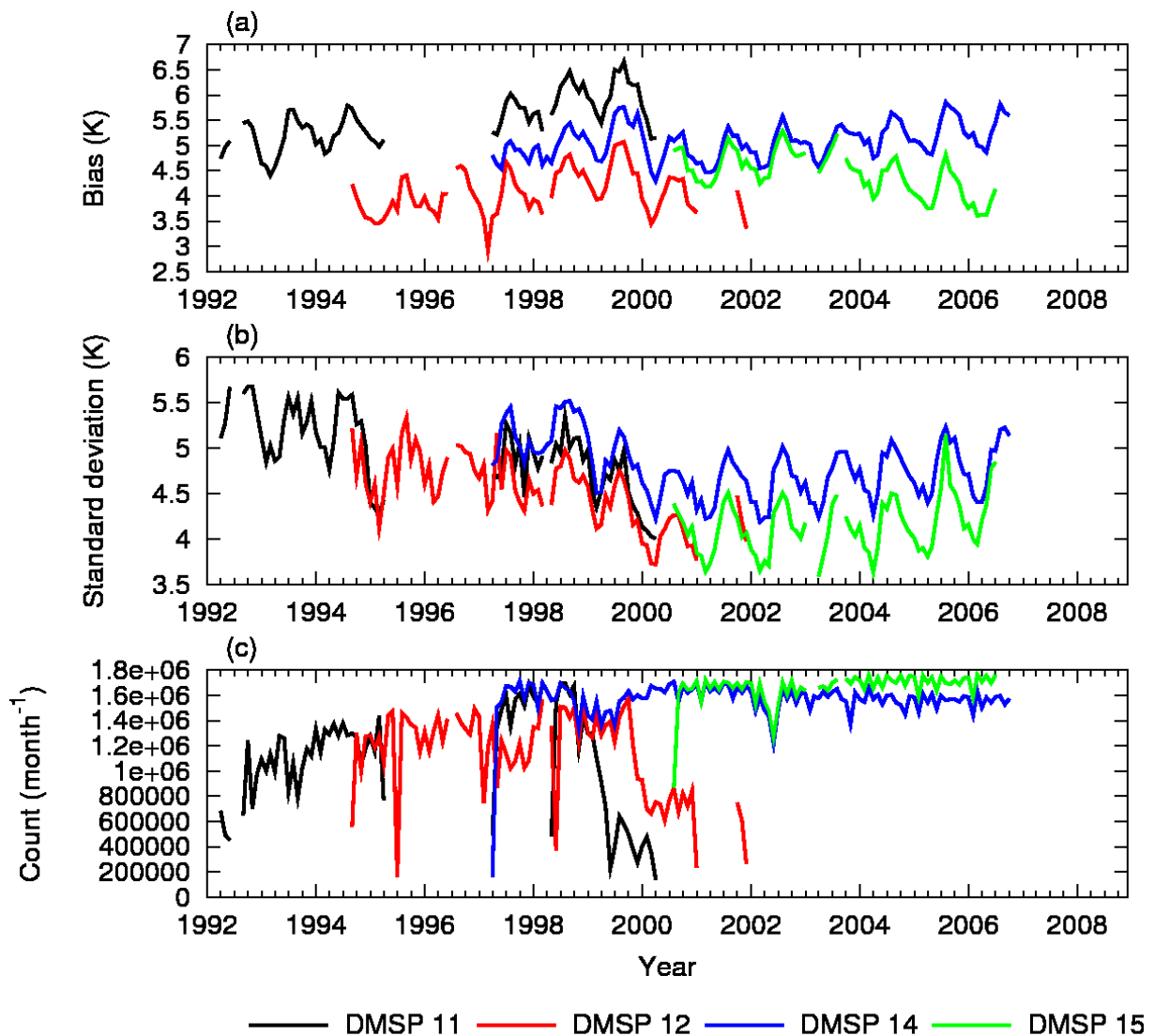


Figure 18. As Figure 12, but for the second computations.

## 6 Conclusions and recommendations

In this study, SSM/T-2 radiances are characterised using ERA-Interim and other reanalyses. The results have confirmed that the SSM/T-2 measurements maintain a sufficient stability to consider using them with similar measurements from AMSU-A, MHS and ATMS for climate applications. The study has also revealed the following issues that need to be taken into account when producing FCDRs from the SSM/T-2 measurements, or assimilating them into future reanalyses.

For the radiative transfer model, the polarisation state of the SSM/T-2 is examined by comparing observations and simulations for the window channels. The result confirms the conclusion of Burns *et*

*al.* (1998), i.e., the SSM/T-2 antenna was very likely oriented towards horizontal polarisation in the limit of nadir viewing.

The departures of channel 4, which has a large sensitivity to the surface, from reanalysis calculations reveal that DMSP 14 suffers from large geolocation errors. For SSM/I on DMSP satellites, Berg *et al.* (2013) corrected geolocation errors using more accurate spacecraft ephemeris and sensor mounting angles estimated from differences between brightness temperatures of ascending and descending orbits to produce FCDRs from these data. A similar method might be applicable to address the geolocation errors in SSM/T-2 data. Also, satellite zenith angles are computed from nominal nadir angles and the Earth's radius as an ellipsoid of revolution because the SSM/T-2 input dataset does not contain this information. Recalculation of geolocation could be the occasion to derive more accurate satellite zenith angles.

The measurements at three outermost positions (26-28) on the solar side of the SSM/T-2 on DMSP 11, 14 and 15 are seriously contaminated by the glare obstruction bracket, which was designed to keep sunlight out of the instrument cavity (e.g. Miao *et al.*, 2001). Unless a correction method based on physical principles can be derived, these data should be excluded from further production of CDRs and use in reanalyses. It could be valuable to encourage constructing a computer model of the DMSP spacecrafts to conduct graphical ray-tracing simulations as done by Kunkee *et al.* (2008b) for the SSMIS on DMSP 16 to understand the effect of this obstructor, and also possibly find other explanations for inter-satellite differences.

The brightness temperatures during the period before 1994 contain unphysical values quasi-periodically. Quality flags in the SSM/T-2 dataset are not necessarily set for these poor quality data. Therefore, additional quality control such as departure check is necessary to remove them.

To detect cloud-affected measurements, the cloud filtering method of Buehler *et al.* (2007) for AMSU-B is employed. In the scatter density plots between observed and simulated brightness temperatures, the data after the cloud filtering are in general distributed along the diagonal. However, departures from the diagonal suggest that the cloud filtering method needs to be perfected. For reanalysis applications, an all-sky assimilation scheme, which explicitly takes into account the scattering effect of hydrometeors in radiative transfer simulations, is also worth consideration. In addition, simulated brightness temperatures for window channels are considerably lower than observations, indicating that radiances from the surface are underestimated in the radiative transfer simulations.

Stability of SSM/T-2 measurements is assessed using time series for brightness temperatures and their departures averaged over the tropical ocean. For the tropospheric humidity channels (1-3) of SSMT-2 on DMSP 11, monthly mean departures from the ERA-Interim analysis show a decreasing trend (about 0.5 K in total over the record length). Monthly mean departures of DMSP 12 and 14 are in general stable, but there is a steady difference of 0.5 to 1 K in all channels between them, including during the orbital overlapping period when the two satellites made observations at almost the same local times. This indicates that continuous inter-satellite biases exist between the two satellites. The magnitude of this bias for the upper tropospheric humidity channel (2), at about 1 K in brightness temperature or around 2 % in relative humidity, exceeds inter-annual variations. This mandates correction of biases before using these data directly in climate monitoring applications. Reanalyses may be able to exploit the data with the help of automated or variational bias correction methods that use the other observations

available to discriminate between sources of systematic error. For the channels 2 and 5 of SSM/T-2 on DMSP 14, standard deviations of departures increase after 2001 and 1999 respectively. The measurements from DMSP 15 are unstable for all channels after November 2001 when the measurements of channel 4 degrade significantly. Therefore, great care is needed when using the measurements after this date from DMSP 15 for climate monitoring and reanalyses.

After the completion of the first computations, the entire computations are re-run to apply lessons learnt and correct some of the problems identified in the first computations. The fit between observed and simulated brightness temperatures is improved significantly as a result. For instance, the large biases for the window channels (4, 5) are reduced considerably, and standard deviations for the lower tropospheric humidity channel (3) and the 150 GHz channel (5) are reduced by about 3%. This highlights the importance of accurate reference data and radiative transfer models for error characterisation, and that it is essential to further improve radiative transfer computations through an “iterative process” for better understanding of the error characteristics.

Finally, all the SSM/T-2 data analyzed in this study, along with the radiative transfer simulations, are available to advance research from the ECMWF MARS facility, in the hope that this work will eventually enable the generation of a 183 GHz FCDR.

## **Acknowledgements**

This study was made possible by support from the EUMETSAT CM-SAF visiting scientist programme, and the respective affiliation institutions of the authors. Peter Rayer and the EUMETSAT NWP-SAF are thanked for providing radiative transfer coefficients for SSM/T-2. The authors would also like to thank Roger Saunders and William Ingram for their guidance during the course of this study.

## Appendix A: Parameters contained in SSM/T-2 ODB files

Table A.1 lists the parameters read from SSM/T-2 NetCDF files and written into ODB. Table A.2 lists the feedback columns added from reanalyses and radiative transfer simulations using those profiles. The columns in Table A.2 were added for both ERA-Interim and ERA-20C, and <FB> represents “@ei” and “@e2oper” respectively.

Table A.1. List of parameters read from SSM/T-2 NetCDF files and written into ODB

ODB column name	Contents	Unit or format	Origin	Range
expver@desc	MARS attribute			1936
type@desc	MARS attribute			263
class@desc	MARS attribute			22
stream@desc	MARS attribute			1025
andate@desc	MARS attribute	YYYYMMDD	Calculated from 'ancil_data'	19920412 to 20080528
antime@desc	MARS attribute	HH*10000	Calculated from 'ancil_data'	0, 60000, 120000, 180000
seqno@hdr	ODB record number	Integer	Counter	>=1
collection_identifier@hdr	Traceability to input NetCDF filename	HHMMSN or -1HHMMSN	HHMM: hour and minute of input NetCDF filename SN: satellite number of input NetCDF filename (11, 12, 14, 15) Date of input NetCDF filename: date@hdr for HHMMSN the day before date@hdr for -1HHMMSN	
date@hdr	Observation date	YYYYMMDD	Calculated from 'ancil_data'	19920412 to 20080528
time@hdr	Observation time	HHMMSS	Calculated from 'ancil_data'	0-235959
lat@hdr	Observation latitude	degreesNorth	'lat'	
lon@hdr	Observation longitude	degreesEast	'lon'	-180 to 180
stalt@hdr	Spacecraft altitude	km	'ancil_data'	
reportype@hdr	MARS attribute		Determined from satellite number	58001 for DMSP 11 58002 for DMSP 12 58003 for DMSP 14 58004 for DMSP 15
bufrtype@hdr	IFS attribute			3
subtype@hdr	IFS attribute			55
groupid@hdr	MARS attribute			59
obstype@hdr	IFS attribute			7
codetype@hdr	IFS attribute			210
sensor@hdr	RTTOV attribute			33
source@hdr	Traceability attribute			'EUMSSMT2'
satellite_identifier@sat	WMO attribute			244, 245, 247, 248
satellite_instrument@sat	WMO attribute			907

ODB column name	Contents	Unit or format	Origin	Range
zenith@sat	Satellite zenith angle	degrees	Calculated from nadir angle and satellite altitude	
azimuth@sat	Satellite azimuth angle	degrees	Calculated from 'ancil_data:SatHeading'	0 to 360
scanline@radiance	IFS attribute			>=1
scanpos@radiance	Scan position			1 to 28
entryno@body	ODB entry number within record			
unique_identifier@body	Traceability to input data	$(i\_time\_step * 28 + i\_scan\_position) * 5 + i\_channel$	i_time_step=index for 'time_step' i_scan_position=index for 'scan_position' i_channel=index for 'channel'	
vertco_reference_1@body	Channel number			
vertco_type@body	IFS attribute			3
verno@body	IFS attribute			119
obsvalue@body	Observed brightness temperature	K	'tb'	
datum_qcflag@body	Quality flag		'channel_quality_flag'	0=not QC 1=artificial 2=questionable 4=LS bit problem
si150@body	Scattering index of Ferraro <i>et al.</i> (2000)	K	'tb(4)':'tb(5)'	
filter_1ghz@body	Cloud filter of Buehler <i>et al.</i> (2007)	K	'tb(2)'	
filter_31ghz@body	Cloud filter of Buehler <i>et al.</i> (2007)	K	'tb(1)':'tb(2)'	
filter_71ghz@body		K	'tb(3)':'tb(2)'	
filter_73ghz@body	Cloud filter of Buehler <i>et al.</i> (2007)	K	'tb(3)':'tb(1)'	

Table A.2. List of added feedback columns

ODB column name	Contents	Unit or format	Range
elev<FB>	Surface elevation	m	
lsm<FB>	Land-sea mask		From 0.0 for sea-only to 1.0 for land-only
skt<FB>	Skin temperature	K	
ice<FB>	Sea-ice cover		0. no ice, 1. fully covered by sea-ice
fgbt<FB>	Brightness temperature calculated by RTTOV	K	
fg_depar<FB>	Observation minus RTTOV simulation	K	
emis_fg<FB>	Surface emissivity		Estimated with FASTEM-5 over sea, and assumed to be 0.95 over land and 0.9 over sea-ice respectively

## Appendix B: Access to SSM/T-2 ODB files

The feedback information derived in this study from the second set of computations, together with the original SSM/T-2 data, is archived in the ECMWF MARS archive in the ODB format. MARS users can either access the data from an ECMWF workstation or via the internet at <http://apps.ecmwf.int/services/mars/catalogue/mars?type=ofb&class=e2&stream=oper&expver=1936>, though the latter method does not have the full functionality of the former method. Full documentation for MARS can be found at <http://www.ecmwf.int/en/what-mars>.

The following examples show how SSM/T-2 ODB files can be extracted from the MARS archive to an ECMWF workstation.

- Example 1: extracting all columns of data from DMSP 11

Retrieve, Class=e2, Expver=1936, Stream=oper, Type=ofb, Reporttype=58001, Date=19930101, Time=all, Target=myfile.odb

- Example 2: extracting all columns of data from DMSP 12

Retrieve, Class=e2, Expver=1936, Stream=oper, Type=ofb, Reporttype=58002, Date=20010101, Time=all, Target=myfile.odb

- Example 3: extracting all columns of data from DMSP 14

Retrieve, Class=e2, Expver=1936, Stream=oper, Type=ofb, Reporttype=58003, Date=20010101, Time=all, Target=myfile.odb

- Example 4: extracting all columns of data from DMSP 15

Retrieve, Class=e2, Expver=1936, Stream=oper, Type=ofb, Reporttype=58004, Date=20010101, Time=all, Target=myfile.odb

- Example 5: extracting select columns of data from DMSP 11 with quality flag set to 0

Retrieve, Class=e2, Expver=1936, Stream=oper, Type=ofb, Reporttype=58001, Date=19930101, Time=all, Target=myfile.odb, Filter="select andate, antime, collection\_identifier, date, time, lat, lon, scanpos, unique\_identifier, vertco\_reference\_1, obsvalue, si150, filter\_1ghz, filter\_31ghz, filter\_71ghz, filter\_73ghz, elev@ei, lsm@ei, skt@ei, ice@ei, fgbt@ei, fg\_depar@ei, emis\_fg@ei, elev@e2oper, lsm@e2oper, skt@e2oper, ice@e2oper, fgbt@e2oper, fg\_depar@e2oper, emis\_fg@e2oper where datum\_qcflag=0"

- Example 6: extracting select columns of data from DMSP 12 with quality flag set to 0

Retrieve, Class=e2, Expver=1936, Stream=oper, Type=ofb, Reporttype=58002, Date=20010101, Time=all, Target=myfile.odb, Filter="select andate, antime, collection\_identifier, date, time, lat, lon, scanpos, unique\_identifier, vertco\_reference\_1, obsvalue, si150, filter\_1ghz, filter\_31ghz, filter\_71ghz, filter\_73ghz, elev@ei, lsm@ei, skt@ei, ice@ei, fgbt@ei, fg\_depar@ei, emis\_fg@ei, elev@e2oper, lsm@e2oper, skt@e2oper, ice@e2oper, fgbt@e2oper, fg\_depar@e2oper, emis\_fg@e2oper where datum\_qcflag=0"

- Example 7: extracting select columns of data from DMSP 14 with quality flag set to 0

Retrieve, Class=e2, Expver=1936, Stream=oper, Type=ofb, Reporttype=58003, Date=20010101, Time=all, Target=myfile.odb, Filter="select andate, antime, collection\_identifier, date, time, lat, lon, scanpos, unique\_identifier, vertco\_reference\_1, obsvalue, si150, filter\_1ghz, filter\_31ghz, filter\_71ghz, filter\_73ghz, elev@ei, lsm@ei, skt@ei, ice@ei, fgbt@ei, fg\_depar@ei, emis\_fg@ei, elev@e2oper, lsm@e2oper, skt@e2oper, ice@e2oper, fgbt@e2oper, fg\_depar@e2oper, emis\_fg@e2oper where datum\_qcflag=0"

- Example 8: extracting select columns of data from DMSP 15 with quality flag set to 0

Retrieve, Class=e2, Expver=1936, Stream=oper, Type=ofb, Reporttype=58004, Date=20010101, Time=all, Target=myfile.odb, Filter="select andate, antime, collection\_identifier, date, time, lat, lon, scanpos, unique\_identifier, vertco\_reference\_1, obsvalue, si150, filter\_1ghz, filter\_31ghz, filter\_71ghz, filter\_73ghz, elev@ei, lsm@ei, skt@ei, ice@ei, fgbt@ei, fg\_depar@ei, emis\_fg@ei, elev@e2oper, lsm@e2oper, skt@e2oper, ice@e2oper, fgbt@e2oper, fg\_depar@e2oper, emis\_fg@e2oper where datum\_qcflag=0"

## Appendix C: Blacklisted periods

The data in the following periods are not used in this study due to quality issues described below:

- SSM/T-2 on DMSP 11:

Channel 5 after 20 June 1993, most likely due to failure of the 75 GHz Gunn diode oscillator (Kieu *et al.*, 1994).

- SSM/T-2 on DMSP 15:

All channels from 25 December 2000, 21 UTC to 26 December 2000, 21 UTC, due to large noise.

Channel 5 after November 2001, due to unstable radiances (Chung and John, 2013).

Channel 4 from February to March, and in September 2003, due to large noise.

Channel 4 after 14 August 2006, due to interference from a radar calibration beacon ([http://nsidc.org/data/docs/daac/f15\\_platform.gd.html](http://nsidc.org/data/docs/daac/f15_platform.gd.html)).

## References

Berg W, Sappiano MRP, Horsman J, Kummerow C. 2013. Improved geolocation and earth incidence angle information for a fundamental climate data record of the SSM/I sensors. *IEEE Trans. Geosci. Remote Sens.* 51: 1504-1513.

Buehler SA, John VO. 2005. A simple method to relate microwave radiances to upper tropospheric humidity. *J. Geophys. Res.* 110, D02110, DOI:10.1029/2004JD005111.

Buehler SA, Kuvatov M, Sreerexha TR, John VO, Rydberg B, Eriksson P, Notholt J. 2007. A cloud filtering method for microwave upper tropospheric humidity measurements. *Atmos. Chem. Phys.* 7: 5531-5542.

- Burns BA, Wu X, Diak GR. 1998. Impact of emissivity model errors on retrieval of water vapor profiles over ocean with SSM/T2. 1998 IEEE International Geoscience and Remote Sensing Symposium Proceedings. Seattle, USA, 6-10 July 1998, 2171-2174.
- Chung E-S, John VO. 2013. Initial assessment of SSM/T-2 radiances. CM SAF Visiting Scientist activity No. 12.02.
- Dee DP, Uppala SM, Simmons AJ, Berrisford P, Poli P, Kobayashi S, Andrae U, Balmaseda MA, Balsamo G, Bauer P, Bechtold P, Beljaars ACM, van de Berg L, Bidlot J, Bormann N, Delsol C, Dragani R, Fuentes M, Geer AJ, Haimberger L, Healy SB, Hersbach H, Hólm EV, Isaksen L, Kállberg P, Köhler M, Matricardi M, McNally AP, Monge-Sanz BM, Morcrette J-J, Park B-K, Peubey C, de Rosnay P, Tavolato C, Thépaut J-N, Vitart F. 2011. The ERA-Interim reanalysis: configuration and performance of the data assimilation system. *Q. J. R. Meteorol. Soc.* 137: 553-597.
- Falcone VJ, Griffin MK, Isaacs RG, Pickle JD, Morrissey JF, Jackson AJ, Bussey A. 1992. SSM/T-2 calibration and validation data analysis. Environ. Res. Papers, 1111, Phillips Laboratory, Hanscom Air Force Base, USA,
- Felde GW, Pickle JD. 1995. Retrieval of 91 and 150 GHz Earth surface emissivities. *J. Geophys. Res.* 100. D10: 20855-20866.
- Ferraro RR, Weng F, Grody NC, Zhao L. 2000. Precipitation characteristics over land from the NOAA-15 AMSU sensor. *Geophys. Res. Lett.* 27: 2669-2672.
- Galín I, Brest DH, Martner GR. 1993. The DMSP SSM/T-2 microwave water-vapor profiler. *SPIE Proceedings.* 1935: 189-198.
- Gorobets NN, Cherny IV, Chernyavsky GM, Barsukov IA. 2007. Microwave Imager/Sounder *MTVZAGY* of spacecraft "Meteor-M". *MSMW'07 Symposium Proceedings.* Kharkov, Ukraine, June 25-30. 2007, 772-774.
- Hartmann DL, Klein Tank AMG, Rusticucci M, Alexander LV, Brönnimann S, Charabi Y, Dentener FJ, Dlugokencky EJ, Easterling DR, Kaplan A, Soden B, Thorne PW, Wild M, Zhai PM. 2013. Observations: Atmosphere and surface. In: *Climate Change 2013: The Physical Science Basis. Contribution of Working Group I to the Fifth Assessment Report of the Intergovernmental Panel on Climate Change* [Stocker TF, Qin D, Plattner G-K, Tignor M, Allen SK, Boschung J, Nauels A, Xia Y, Bex V, Midgley PM (eds.)]. Cambridge University Press, Cambridge, United Kingdom and New York, NY, USA.
- Hilburn KA, Wentz FJ. 2008. Mitigating the impact of RADCAL beacon contamination on F15 SSM/I ocean retrievals. *Geophys. Res. Lett.*, 35, L18806, DOI:10.1029/2008GL034914.
- John VO, Holl G, Allan RP, Buehler SA, Parker DE, Soden BJ. 2011. Clear-sky biases in satellite infrared estimates of upper tropospheric humidity and its trends. *J. Geophys. Res.* 116:D14108. DOI:10.1029/2010JD015355.
- Kakar RK. 1983. Retrieval of clear sky moisture profiles using the 183 GHz water vapor line. *J. Climate Appl. Meteor.*, 22, 1282–1289. DOI:10.1175/1520-0450(1983)022<1282:ROCSMP>2.0.CO;2.

- Kieu D, Stogryn A, Goe G, Kreiss W, Dickey R. 1994. The performance of the SSM/T-2 moisture sensor on DMSP S12: Part II: Post-June 1993 anomaly. *SPIE Proceedings*. 2222: 45-54.
- Kobayashi S, Ota Y, Harada Y, Ebata A, Moriya M, Onoda H, Onogi K, Kamahori H, Kobayashi C, Endo H, Miyaoka K, Takahashi K. 2015. The JRA-55 reanalysis: General specifications and basic characteristics. *J. Meteor. Soc. Japan*. 93: DOI:10.2151/jmsj.2015-001.
- Kunkee, DB, Poe GA, Boucher DJ, Swadley SD, Hong Y, Wessel JE, Uliana EA. 2008a. Design and evaluation of the first Special Sensor Microwave Imager/Sounder. *IEEE Trans. Geosci. Remote Sens.* 46:4. DOI: 10.1109/TGRS.2008.917980.
- Kunkee, DB, Swadley SD, Poe GA, Hong Y, Werner MF. 2008b. Special Sensor Microwave Imager Sounder (SSMIS) radiometric calibration anomalies-Part I: Identification and characterization. *IEEE Trans. Geosci. Remote Sens.* 46:4. DOI:10.1109/TGRS.2008.917213.
- Liu Q, Weng F, English SJ. 2011. An improved fast microwave water emissivity model. *IEEE Trans. Geosci. Remote Sens.* 49: 1238-1250.
- Lu Q, Bell W, Bauer P, Bormann N, Peubey C. 2011. Characterizing the FY-3A microwave temperature sounder using the ECMWF model. *J. Atmos. Oceanic Technol.* 28: 1373-1389.
- Lu Q, Bell W. 2014. Characterizing channel center frequencies in AMSU-A and MSU microwave sounding instruments. *J. Atmos. Oceanic Technol.* 31: 1713-1732.
- Miao J, Kunzi K, Heygster G. 2001. Atmospheric water vapor over Antarctica derived from Special Sensor Microwave/Temperature 2 data. *J. Geophys. Res.* 106, D10: 10187-10203.
- Moradi I, Meng H, Ferrano RR, Bilanow S. 2013. Correcting geolocation errors for microwave instruments aboard NOAA satellites. *IEEE Trans. Geosci. Remote Sens.* 51: 3625-3637.
- Poli P. 2010. List of observations assimilated in ERA-40 and ERA-Interim (v1.0). ERA Report Series, 4, ECMWF, UK, 25pp. Available at <http://www.ecmwf.int/en/research/publications/>.
- Poli P, Hersbach H, Tan D, Dee D, Thépaut J-N, Simmons A, Peubey C, Laloyaux P, Komori T, Berrisford P, Dragani R, Trémolet Y, Hólm E, Bonavita M, Isaksen L, Fisher M. 2013. The data assimilation system and initial performance evaluation of the ECMWF pilot reanalysis of the 20th-century assimilating surface observations only (ERA-20C). ERA Report Series. 14. ECMWF. UK. 59pp. Available at <http://www.ecmwf.int/en/research/publications/>.
- Poli P, Peubey C, Fennig K, Schröder M, Roebeling R, Geer A. 2015. Pre-assimilation feedback on a Fundamental Climate Data Record of brightness temperatures from Special Sensor Microwave Imagers: A step towards MIPs4Obs? ERA Report Series. 19. ECMWF. UK. 50pp. Available at <http://www.ecmwf.int/en/research/publications/>.
- Robel J (ed.), 2009. NOAA KLM user's guide with NOAA-N, -N' supplement. February 2009 revision, NOAA, USA. Available at <http://www.ncdc.noaa.gov/oa/pod-guide/ncdc/docs/klm/index.htm>.
- Saunders R, Hocking J, Rundle D, Rayer P, Matricardi M, Geer A, Lupu C, Brunel P, Vidot J. 2013. RTTOV-11 science and validation report. EUMETSAT NWP SAF, 62pp. Available at [http://nwpsaf.eu/deliverables/rtm/rtm\\_rttov11.html](http://nwpsaf.eu/deliverables/rtm/rtm_rttov11.html).

Simmons AJ, Poli P, Dee DP, Berrisford P, Hersbach H, Kobayashi S, Peubey C. 2014. Estimating low-frequency variability and trends in atmospheric temperature using ERA-Interim. *Q. J. R. Meteorol. Soc.* 140: 329-353.

Weng F, Zou X, Sun N, Yang H, Tian M, Blackwell WJ, Wang X, Lin L, Anderson K. 2013. Calibration of Suomi national polar-orbiting partnership advanced technology microwave sounder. *J. Geophys. Res.* 118: 11,187-11,200. DOI: 10.1002/jgrd.50840.

Wessel JE, Boucher D. 1998. Comparison between cross-track and conical scanning microwave window channels near 90 GHz. *IEEE Trans. Geosci. Remote Sens.* 36: 16-24.